

# NanoSD: Edge Efficient Foundation Model for Real Time Image Restoration

Subhajit Sanyal<sup>1\*</sup> Srinivas Soumitri Miriyala<sup>1\*</sup> Akshay Janardan Bankar<sup>1\*</sup>  
 Sravanth Kodavanti<sup>1</sup> Manjunath Arvetti<sup>1</sup> Harshit<sup>1</sup> Abhishek Ameta<sup>1</sup> Shreyas Pandith<sup>1</sup>  
 Amit Satish Unde<sup>1</sup>

<sup>1</sup>Samsung Research India, Bangalore

{a.bankar, srinivas.m1, amit.unde}@samsung.com

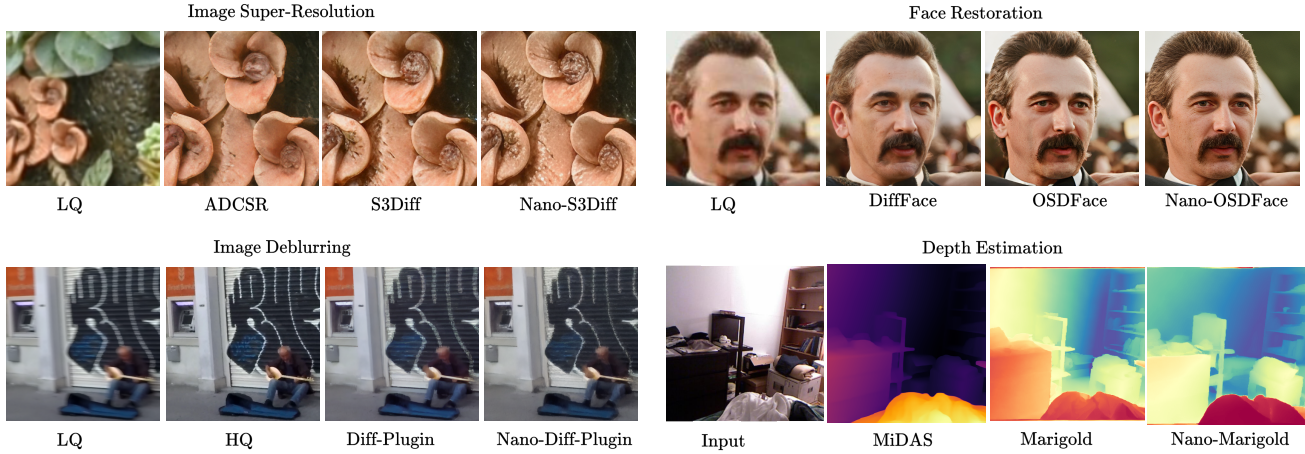


Figure 1. We present NanoSD, an edge-efficient diffusion model designed for image restoration applications. Its core principle is to harness the extensive visual priors embedded in contemporary generative image models while maintaining computational feasibility for edge deployment. NanoSD demonstrates practical applicability across diverse low-level vision tasks in real-world scenarios.

## Abstract

Latent diffusion models such as Stable Diffusion 1.5 offer strong generative priors that are highly valuable for image restoration, yet their full pipelines remain too computationally heavy for deployment on edge devices. Existing lightweight variants predominantly compress the denoising U-Net or reduce the diffusion trajectory, which disrupts the underlying latent manifold and limits generalization beyond a single task. We introduce NanoSD, a family of Pareto-optimal diffusion foundation models distilled from Stable Diffusion 1.5 through network surgery, feature-wise generative distillation, and structured architectural scaling jointly applied to the U-Net and the VAE encoder-decoder. This full-pipeline co-design preserves the generative prior while producing models that occupy distinct operating points along the accuracy-latency-size

frontier (e.g., 130M–315M parameters, achieving real-time inference down to 20ms on mobile-class NPUs). We show that parameter reduction alone does not correlate with hardware efficiency, and we provide an analysis revealing how architectural balance, feature routing, and latent-space preservation jointly shape true on-device latency. When used as a drop-in backbone, NanoSD enables state-of-the-art performance across image super-resolution, image deblurring, face restoration, and monocular depth estimation, outperforming prior lightweight diffusion models in both perceptual quality and practical deployability. NanoSD establishes a general-purpose diffusion foundation model family suitable for real-time visual generation and restoration on edge devices.

\*Equal contribution

## 1. Introduction

Image restoration (IR) focuses on reconstructing high-quality (HQ) images from their degraded low-quality (LQ) counterparts [26, 35, 61]. Recent advancements in diffusion model (DM) acceleration have garnered significant interest, particularly in the context of image super-resolution (SR) [5, 12, 44]. While several one-step diffusion-based approaches have demonstrated promising results, their computational complexity remains prohibitive for real-world deployment [44, 47, 55]. To address these challenges, recent research has prioritized architectural optimizations to reduce redundancy in large-scale models [6, 23]. Although these methods maintain strong generation capabilities for text-to-image (T2I) tasks, their practical deployment on computationally limited platforms faces substantial hurdles due to excessive model sizes and latency [23, 60]. These limitations are further compounded in IR, which inherently operates on high-resolution inputs and often requires multiple model executions [12].

To enable the practical deployment of diffusion-based restoration on edge devices, several distillation techniques have been explored, particularly for SR tasks [8, 12, 39]. While these methods demonstrate promising efficiency gains, they are primarily optimized for SR tasks using limited datasets, preventing them from fully leveraging the rich prior knowledge encoded in large pre-trained T2I models. Consequently, such distilled models often produce structurally implausible results with perceptually suboptimal details. Additionally, existing methods lack the flexibility to accommodate diverse conditioning strategies required for broader IR tasks [5, 8, 12, 39]. For example, S3Diff [55] incorporates a degradation-aware Low-Rank Adaptation (LoRA) module, while OSDFace [41] utilizes visual prompts as supplementary conditioning. Similarly, Diff-Plugin [26] introduces a lightweight task-specific module via cross-attention mechanisms, and DiffBIR [25] employs a ControlNet-based [58] architecture for image conditioning. These specialized approaches highlight the need for a versatile framework for edge-efficient diffusion methods to support a wider range of restoration scenarios.

Designing edge-efficient diffusion models for diverse restoration tasks hinges on effectively integrating conditional information to guide accurate and natural outputs—an aspect often overlooked in prior work. Also, since modern diffusion models are pretrained on large-scale datasets, preserving their latent space is crucial. This paper introduces NanoSD, a latent diffusion model based on the Stable Diffusion 1.5 (SD 1.5) [35], optimized for edge efficiency while ensuring compatibility with various control plugins. Our contributions in this paper are as follows:

- We introduce a hardware-aware reformulation of the SD 1.5 U-Net by decomposing it into stage-wise dimensions and constructing a compact set of shape-preserving block variants tailored to edge accelerators.

- We propose a block-level generative distillation strategy that aligns each candidate block variant with its SD 1.5 teacher counterpart, enabling large-scale architectural exploration without full-model retraining.
- We cast the selection of an efficient diffusion backbone as a multi-objective optimization problem over teacher-aligned Fréchet Inception Distance (FID), on-device latency, and parameter count, and employ Bayesian optimization to obtain a Pareto set of U-Nets capturing diverse accuracy–efficiency trade-offs.
- From this Pareto frontier, we identify a balanced architecture—*NanoSD*—and distill the corresponding VAE encoder and decoder to construct a fully lightweight latent diffusion pipeline.
- Through extensive experiments across super-resolution, face restoration, deblurring, dehazing, deraining, desnowing, and monocular depth estimation, we demonstrate that NanoSD maintains the generative behavior of SD 1.5 while substantially reducing computational cost, enabling practical deployment on mobile-class NPUs.

## 2. Related Work

Significant progress in diffusion models, particularly for text-to-image (T2I) synthesis (e.g., SD [35], SD3 [10]), has spurred the development of pre-trained diffusion-based image restoration techniques such as StableSR [40], Diff-Plugin [26], DiffPIR [62], DiffBIR [25], PASD [50], and SeeSR [48]. These methods leverage the robust priors of T2I models, but suffers from substantial latency and computational overhead. To mitigate this, recent efforts focus on single-step frameworks, primarily targeting SR. For instance, SinSR [44] accelerates ResShift [53] via bidirectional distillation, while OSEDiff [47] employs variational score distillation approach to enhance the realism of super-resolved outputs. Building on distilled SD-Turbo architectures, S3Diff [55] integrates a degradation-guided LoRA module to improve SR quality. Albeit promising, high computational cost of these networks hinder their practical deployment on resource-constrained devices.

Recent research in efficient diffusion models has prioritized architectural optimizations. SnapFusion [23] analyzes individual module contributions to balance efficiency and accuracy, while MobileDiff [60] relocates Transformer blocks to lower-resolution stages for computational savings. SnapGen [6] further reduces model size and computation by eliminating high-resolution attention and replacing standard convolutions with depthwise separable variants. Deployment of these methods for high-resolution image restoration remains challenging due to latency constraints. To enhance edge efficiency for SR, AdcSR [5] leverages adversarial diffusion compression to distill OSEDiff [47], significantly re-

ducing complexity by pruning the VAE encoder and denoising UNet. Edge-SD-SR [12] introduces a novel conditioning mechanism for low-resolution inputs, while TinySR [8] employs depthwise UNet pruning and conditional information removal to improve efficiency. PocketSR [39] adopts multi-layer feature distillation for enhanced knowledge transfer. However, current edge-efficient models underutilize the generative capabilities of T2I frameworks and lack modular support for advanced conditioning mechanisms (e.g., LoRA [47, 55], ControlNet [25]), limiting their applicability to diverse restoration tasks [26, 41].

### 3. Method

Our objective is to derive an edge-efficient diffusion foundation model from SD 1.5 baseline [35]. Although SD 1.5 provides strong generative priors, its U-Net and VAE components remain prohibitively heavy for embedded NPUs. Moreover, theoretical compute metrics (FLOPs/GMACs) do not reliably predict practical latency, since NPUs are optimized for specific operator patterns (e.g., GEMM), tensor layouts, and memory behavior. As a result, reducing arithmetic compute alone does not guarantee proportional latency improvements. To address this mismatch, we introduce a hardware-aware architectural redesign and distillation framework (Fig. 2) that restructures SD 1.5 at the block level, constructs a tractable search space aligned with edge hardware (Fig. 2b), trains locally distilled surrogate blocks that preserve SD 1.5’s generative behavior (Fig. 2c), and selects full U-Net architectures using multi-objective Bayesian optimization (Fig. 2d). This search over the distilled block variants produces a Pareto-optimal set of U-Net backbones, each representing a different accuracy–efficiency trade-off. From this set, we select a single U-Net that offers the most balanced operating point and fix it as our base architecture *NanoSD*. Keeping this U-Net frozen, we then distill the corresponding VAE encoder and decoder from SD 1.5, yielding a fully lightweight latent diffusion pipeline tailored to the selected U-Net.

#### 3.1. Hardware-Aware Decomposition of U-Net

The SD 1.5 U-Net consists of four encoders, a middle block, and four decoders. Prior analyses in lightweight diffusion literature—including SnapFusion [23], Segmind TinySD [19], and Koala [20]—report that the deepest encoder (encoder-4), the adjacent middle block, and the corresponding decoder-4 contribute minimally to generative fidelity. Motivated by these findings, we remove these three stages entirely from our design space. The remaining backbone comprises three encoders and three decoders, each treated as an independent architectural dimension.

For each stage, we inspect the original SD 1.5 block structure and derive hardware-friendly variants that strictly preserve input/output tensor shapes. For example, the

SD 1.5 block in the first decoder stage contains a sequence of residual and attention modules followed by a convolution, denoted R–A–R–A. We construct shape-preserving variants (e.g., residual-only or reduced-attention configurations) such that all alternatives remain strictly compatible with upstream and downstream tensors. Applying this procedure to all six stages yields the full combinatorial design space illustrated in Fig. 2a and Fig. 2b. The resulting space consists of 32,768 ( $4 \times 4 \times 4 \times 8 \times 8 \times 8$ ) candidate U-Net architectures, each of which is dimensionally valid without requiring adapters or tensor reshaping.

#### 3.2. Feature-Wise Generative Distillation

Training all 32,768 architectures end-to-end is infeasible. We therefore adopt a divide-and-conquer distillation strategy at the block level. For a given stage  $i$  and candidate variant  $j$ , let  $\mathcal{B}_i$  denote the SD 1.5 block (teacher) and  $\mathcal{B}_{i,j}$  the corresponding variant (student). For input features  $F$ , the teacher and student outputs are

$$O_T = \mathcal{B}_i(F), \quad O_S = \mathcal{B}_{i,j}(F). \quad (1)$$

Each variant is trained with the feature-matching objective

$$\mathcal{L}_{\text{distill}}^{(i,j)} = \|O_S - O_T\|_2^2. \quad (2)$$

Since all blocks are distilled independently, this process is massively parallel and computationally lightweight. Across the six stages, we obtain 30 ( $3+3+3+7+7+7$ ) distilled surrogate blocks (see Supplementary Material for details on training). This preserves SD 1.5’s local generative behavior, enabling full U-Nets assembled from these surrogates to approximate SD 1.5 without full-network training.

#### 3.3. Assembling Candidate Diffusion U-Nets

A complete U-Net architecture is encoded by a discrete vector  $\mathbf{z} = [z_1, z_2, z_3, z_4, z_5, z_6]$ , where each element selects one surrogate block for the corresponding stage. Because all variants maintain spatial and channel compatibility, substituting blocks according to  $\mathbf{z}$  yields a structurally valid U-Net. Combined with the original SD 1.5 VAE encoder and decoder, this produces a functional latent diffusion pipeline, evaluated using the procedure outlined in Fig. 2d.

#### 3.4. Optimization in the H/W-Aligned Space

To measure fidelity, we construct a test dataset of prompts and corresponding SD 1.5 outputs. For any architecture  $\mathbf{z}$ , we generate outputs  $\hat{X}(\mathbf{z})$  using the same prompts and compute the FID:

$$f_{\text{FID}}(\mathbf{z}) = \text{FID}\left(\hat{X}(\mathbf{z}), X_{\text{SD1.5}}\right), \quad (3)$$

which quantifies deviation from SD 1.5’s generative distribution. We report this as a teacher-aligned Fréchet Inception Distance (taFID), as it measures the distributional divergence between the distilled model and the SD 1.5 teacher

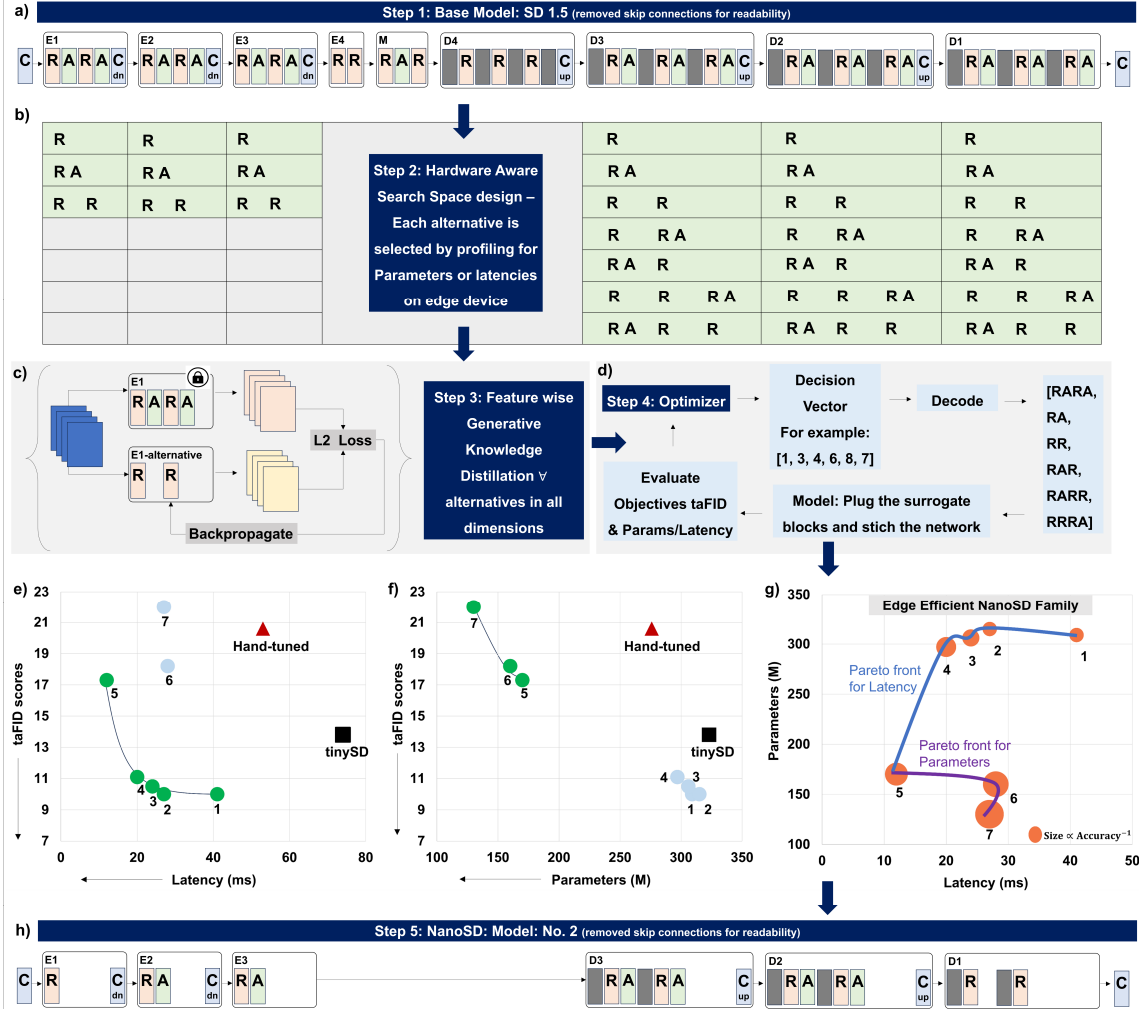


**Figure 2. Overview of the NanoSD framework.** (a) Baseline SD 1.5 U-Net architecture, shown with skip connections removed for readability. (b) Hardware-aware search space construction: for each of the six retained stages (three encoders and three decoders), we derive shape-preserving residual/attention variants that are profiled on the target edge device for latency and parameter cost. (c) Feature-wise generative distillation: each candidate block is distilled independently from its corresponding SD 1.5 teacher block using an  $\ell_2$  feature-matching loss. (d) Combinatorial assembly and evaluation: a decision vector specifies one distilled block per stage, producing a structurally valid U-Net; each assembled model is evaluated on taFID and either on-device latency or parameter count via Bayesian optimization. (e) Latency–taFID Pareto frontier obtained from the search; green points denote Pareto-optimal models, and non-Pareto points are shown for comparison. (f) Parameter–taFID Pareto frontier. Both plots also include a hand-tuned baseline and the Segmind TinySD model, which fall far from the frontier. (g) The resulting *NanoSD family*: seven Pareto-optimal architectures spanning different accuracy–efficiency trade-offs (bubble size inversely proportional to accuracy). (h) Final selected architecture, *NanoSD* (Model 2), used for all downstream experiments; skip connections are omitted for clarity.

using identical prompt–seed pairs, serving as a relative fidelity metric rather than a canonical dataset FID.

To assess efficiency, we consider both parameter count and on-device latency as separate second objectives:

$$f_{\text{param}}(\mathbf{z}), \quad f_{\text{latency}}(\mathbf{z}). \quad (4)$$

This yields two bi-objective problems:

$$\min_{\mathbf{z}} (f_{\text{FID}}(\mathbf{z}), f_{\text{param}}(\mathbf{z})), \quad (5)$$

$$\min_{\mathbf{z}} (f_{\text{FID}}(\mathbf{z}), f_{\text{latency}}(\mathbf{z})), \quad (6)$$

with  $\mathbf{z}$  constrained to the discrete space defined by Fig. 2b.

Because FID evaluation remains costly even without training, we adopt Bayesian Optimization (BO). We relax  $\mathbf{z}$  to a continuous representation  $\mathbf{x} \in [0, 1]^6$  and project it to the nearest feasible architecture via a deterministic mapping. Gaussian Process models approximate both objectives, and candidate points are selected by maximizing Ex-

Table 1. **Comparison of TinySD (Segmind), hand-tuned baseline, and NanoSD variants.** Latency is measured on a Qualcomm NPU using 8-bit weights and 16-bit activations. taFID denotes the teacher-aligned FID metric used during the search. The seven NanoSD models correspond to all Pareto-optimal architectures obtained from the latency–taFID and parameter–taFID objectives. For each model, we list the selected block variants across the retained stages of the SD 1.5 U-Net (E1–E3 for encoders and D3–D1 for decoders). Model 5 achieves the lowest latency, Model 7 achieves the fewest parameters, and Model 2 provides the best overall balance of accuracy and efficiency and is used as *NanoSD* in all downstream experiments.

Model	Latency (ms)	Parameters (M)	taFID	E1	E2	E3	D3	D2	D1
<b>TinySD</b>	74	323	13.8	RA	RA	RA	RA	RA	RA
<b>Hand-tuned</b>	53	276	20.6	RA	RA	RA	RAR	RAR	RAR
<b>NanoSD 1</b>	41	309	10	R	RA	RA	RARA	RRA	RRA
<b>NanoSD 2</b>	27	315	10	R	RA	RA	RARA	RARA	RR
<b>NanoSD 3</b>	24	306	10.5	R	RA	RA	RARA	RRA	RR
<b>NanoSD 4</b>	20	297	11.1	R	RA	RA	RARA	RR	RR
<b>NanoSD 5</b>	12	170	17.3	R	R	R	RA	RR	RR
<b>NanoSD 6</b>	28	160	18.2	R	R	R	RA	RA	RA
<b>NanoSD 7</b>	27	130	22	R	R	R	R	RA	RRA

pected Hypervolume Improvement (EHVI). Full derivations and analyses are provided in the Supplementary Material. BO yields a sparse Pareto frontier of architectures balancing generative fidelity and hardware efficiency.

### 3.5. VAE Distillation and End-to-End Training

After selecting Pareto-optimal U-Nets, we freeze their weights and distill both the VAE encoder and decoder to reduce overall pipeline size. VAE distillation follows standard feature-matching losses between SD 1.5 teacher outputs and student predictions (details in Supplementary Material). Each resulting pair of distilled U-Net and distilled VAE forms a NanoSD candidate.

To correct accumulated discrepancies from block-level distillation, we fine-tune each NanoSD model using the standard diffusion denoising objective. The resulting NanoSD family is evaluated across super-resolution, face restoration, deblurring, dehazing, deraining, desnowing, and monocular depth estimation, demonstrating that the distilled architectures retain SD 1.5’s generative versatility while enabling practical deployment on edge devices.

## 4. Experiments

### 4.1. Pareto Analysis and Model Selection

We conduct two iterations of multi-objective search corresponding to the formulations described in Sec. 3. In the first iteration, we optimize taFID (our teacher-aligned FID metric; see Supplementary Material) jointly with on-device latency measured on a Qualcomm NPU using 8-bit weights and 16-bit activations. In the second iteration, we optimize taFID jointly with parameter count, which serves as a proxy for on-device memory usage. Fig. 2e and Fig. 2f show the resulting Pareto fronts for the latency–taFID and parameter–taFID objectives, respectively. In both plots,

green circles denote Pareto-optimal points, while the remaining points are included for comparison.

Across the two searches, we obtain seven distinct Pareto-optimal architectures (Table 1). Five models arise from the latency–accuracy front and three from the parameter–accuracy front, with one model appearing in both. Taken together, these architectures constitute the *NanoSD family* and span a diverse set of trade-offs between generative fidelity and hardware efficiency.

Within this family, Model 5 achieves the lowest measured latency and represents the optimal choice when runtime efficiency is prioritized (*NanoSD-Latency*). Model 7 attains the smallest parameter footprint and is preferred under strict memory constraints (*NanoSD-Parameters*). Models 1 and 2 obtain the best taFID values overall with nearly identical accuracy. However, Model 1 incurs substantially higher latency, whereas Model 2 exhibits a more balanced accuracy–efficiency profile with only a marginal increase in parameter count (Table 1). Because the latency difference between Models 1 and 2 is significantly larger than their parameter difference, we select Model 2 as the representative backbone for downstream evaluation and denote it as *NanoSD-Prime*. The remaining models (1, 3, 4, and 6) occupy intermediate regions of the Pareto front and may be adapted to task-specific or resource-specific constraints (e.g., *NanoSD-S*, *NanoSD-XS*).

Fig. 2e and Fig. 2f also include two baselines: a manually designed hand-tuned variant of SD 1.5 and the prior-art Segmind TinySD [19] model. Both baselines lie far outside the Pareto frontier in terms of accuracy–latency and accuracy–parameter trade-offs. The hand-tuned model exhibits moderate latency but significantly worse taFID, indicating that manual structural simplifications fail to preserve the generative prior. TinySD achieves better accuracy but remains considerably slower and larger than all NanoSD

Table 2. Quantitative comparison of different methods on DIV-2K Val [1] dataset. The best, second-best and third-best results are highlighted in red, blue, and green colors, respectively. Refer to Supplemental for detailed analysis.

Method	PSNR↑	SSIM↑	LPIPS↓	FID↓	NIQE↓	MUSIQ↑	Steps	MACs (G)	Para. (M)
Edge-SD-SR [12]	24.10	0.617	0.249	25.37	-	69.58	1	-	169
AdcSR [5]	23.74	0.602	0.285	25.52	4.36	68.00	1	496	456
TinySR [8]	-	0.572	0.279	22.94	4.15	69.90	1	427	341
PocketSR [39]	23.85	0.601	0.280	25.25	4.41	66.38	1	225	146
Nano-OSEDiff (Ours)	24.29	0.628	0.296	27.46	4.92	66.41	1	340	448
Nano-S3Diff (Ours)	23.13	0.573	0.278	22.34	4.09	70.44	1	285	318

Table 3. Quantitative comparison of different methods on synthetic CelebA-Test [15] dataset. The best, second-best and third-best results are highlighted in red, blue, and green colors, respectively. Refer to Supplemental for detailed analysis.

Method	LPIPS↓	DISTS↓	NIQE↓	MUSIQ↑	FID↓	LMD↓	Steps	MACs (G)	Para. (M)
PGDiff [49]	0.386	0.195	4.001	69.56	44.62	7.310	1000	480998	176
DifFace [52]	0.346	0.212	4.638	66.74	49.80	5.475	250	46575	175
DiffBIR [25]	0.374	0.234	6.280	75.63	71.77	5.104	50	24234	1717
OSDFace [41]	0.336	0.177	3.884	75.64	45.41	5.286	1	2465	1887
Nano-DiffBIR (Ours)	0.382	0.212	6.3	76.52	70.89	5.231	50	4734	726
Nano-OSDFace (Ours)	0.341	0.182	3.913	76.01	45.92	5.172	1	479	415

variants.

All seven NanoSD variants are subsequently fine-tuned end-to-end on image–text pairs derived from publicly available web-scale datasets (LAION-style [36]; see Supplementary Material). The final T2I FID scores for each model are reported in the Supplementary Tables. For the remainder of this paper, we adopt *NanoSD-Prime* as our backbone *NanoSD* (architecture shown in Fig. 2h) and evaluate its generalization ability across a broad suite of low-level vision tasks. The generated images using the proposed NanoSD for T2I task are displayed in Fig. 3.

## 4.2. Experimental Settings

**Datasets.** To test effectiveness of the proposed NanoSD, we utilize specific datasets for each low-level task, SR: LS-DIR [24] and the first 10K face images from FFHQ [16], face restoration: FFHQ [16], deblurring: Gopro [30], dehazing: Reside [21], deraining: merged train [54], desnowing: Snow100K [28], monocular depth estimation: Hypersim [34] and Virtual KITTI [3]. For testing, we evaluate on real-world benchmark datasets, SR: DIV2K-Val [1], RealSR [4] and DRealSR [46], face restoration: Wider-Test [61], LFWTest [14], and WebPhoto-Test [43], deblurring: RealBlur-J [33], dehazing: RTTS [22], deraining: real test [42] and desnowing: realistic test [27], monocular depth estimation: NYU<sub>v2</sub> [37] and KITTI [11].

**Evaluation Metrics.** To provide a comprehensive and holistic assessment on the performance of different methods, we employ a range of full-reference and no-reference metrics. PSNR and SSIM [45] (calculated on the Y channel in YCbCr space) are reference-based fidelity measures,



Figure 3. Generated images using edge efficient NanoSD.

while LPIPS [59], DISTS [7] are reference-based perceptual quality measures. FID [13] evaluates the distance of distributions between GT and restored images. NIQE [57] and MUSIQ [18] are no-reference image quality measures. We apply two widely recognized metrics Absolute Mean Relative Error (AbsRel) [31] and  $\delta 1$  accuracy [32] for assessing quality of depth estimation.

## 4.3. Edge Efficient OSEDiff and S3Diff for Single Image Super-resolution

This paper aims to enable real-time super-resolution by effectively harnessing the rich generative priors inherent in pre-trained diffusion models. We validate the efficacy of the proposed foundation model for edge-efficient SR tasks

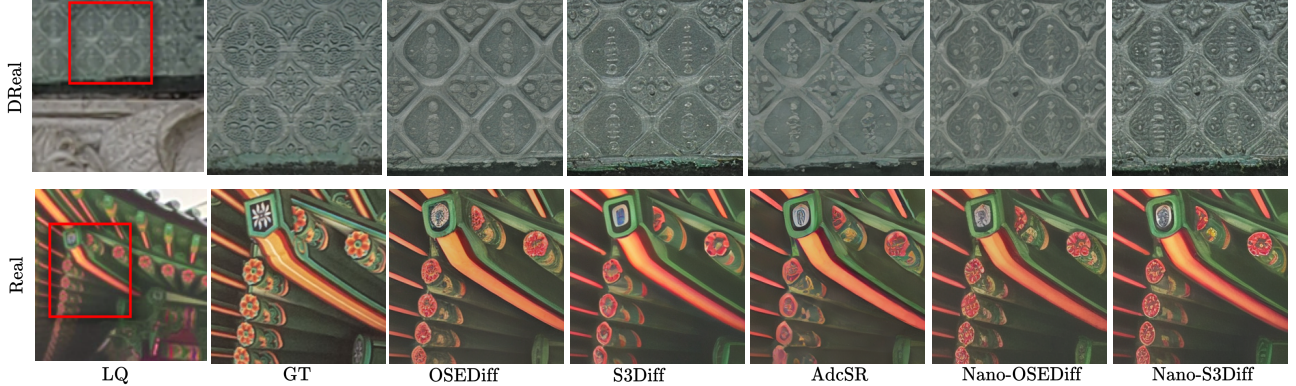


Figure 4. Qualitative comparisons of different SR methods. Please zoom in for a better view. Refer to Supplemental for more results.

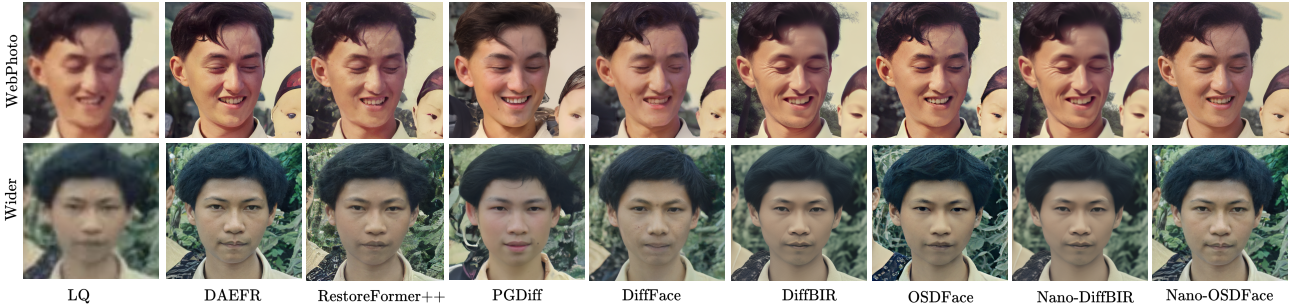


Figure 5. Visual comparisons of various face restoration methods. Please zoom in for a better view. Refer to Supplemental for more results.

by integrating NanoSD with prominent one-step latent diffusion frameworks, namely OSEDiff and S3Diff.

Table 10 presents quantitative comparisons of super-resolution methods across three datasets. Both proposed models exhibit second and third lowest MACs among evaluated approaches, enabling real-time processing and edge deployment. Nano-S3Diff achieves top NIQE and MUSIQ scores, along with second-best FID results, reflecting superior perceptual quality. Meanwhile, Nano-OSEDiff maintains competitive fidelity, yielding the superior PSNR and SSIM performance. Fig. 4 presents qualitative comparisons between different super-resolution methods. Our proposed approaches demonstrate consistent performance in preserving image fidelity and reconstructing fine details.

#### 4.4. Edge Efficient OSDFace for Face Restoration

This section evaluates the applicability of our proposed model for face restoration tasks. To demonstrate its effectiveness, we integrate NanoSD into the OSDFace framework, which represents the current state-of-the-art one-step diffusion approach for face restoration.

Table 3 presents quantitative comparisons on the CelebA-Test dataset. Our proposed Nano-OSDFace

achieves comparable perceptual quality to OSDFace, attaining second-best scores in FID, NIQE, MUSIQ, and LMD which indicates alignment between generated and natural image distributions. The table further highlights Nano-OSDFace’s efficiency, showing significant reduction in computational costs. Figure 5 demonstrates that Nano-OSDFace effectively restores degraded facial inputs without deviating from the identity.

#### 4.5. Accelerating Diff-Plugin and DiffBIR for Image Restoration with Generative Diffusion Prior

The proposed NanoSD is trained on an extensive text-to-image dataset. To leverage its capabilities for diverse low-level vision tasks, we incorporate the model into the Diff-Plugin and DiffBIR frameworks. Both frameworks utilize a pre-trained latent diffusion backbone to adapt to multiple image restoration and enhancement tasks while preserving their inherent generative performance.

Table 4 quantifies the performance of Nano-Diff-Plugin across multiple image restoration tasks. Our model achieves results comparable to state-of-the-art baselines while exhibiting substantial reductions in model size and inference time. Figure 6 illustrates the enhanced performance of

Table 4. Quantitative comparison of different methods on various low-level vision tasks. The best, second-best and third-best results are highlighted in red, blue, and green colors, respectively.

Method	Desnowing Realistic [27]		Dehazing Reside [21]		Deblurring RealBlur-J [33]		Deraining Real Test [42]		Steps	MACs(G)	Para.(M)
	FID $\downarrow$	KID $\downarrow$	FID $\downarrow$	KID $\downarrow$	FID $\downarrow$	KID $\downarrow$	FID $\downarrow$	KID $\downarrow$			
SD [35]	35.24	7.88	48.89	24.47	59.21	18.96	51.78	17.69	200	79940	1410
InstructP2P [2]	42.01	8.54	33.48	12.76	57.38	19.37	54.12	17.87	100	103381	1027
Null-Text [29]	60.49	16.38	39.94	14.88	60.38	20.37	51.49	15.43	50	374137	1027
ControlNet [58]	34.36	5.70	37.02	15.45	52.30	17.19	52.55	15.22	50	24637	1397
Diff-Plugin [26]	34.30	5.20	34.68	14.38	51.81	14.63	50.55	13.84	20	30400	1256
Nano-Diff-Plugin	34.83	5.63	35.23	15.03	52.41	15.48	50.78	14.21	20	17120	712

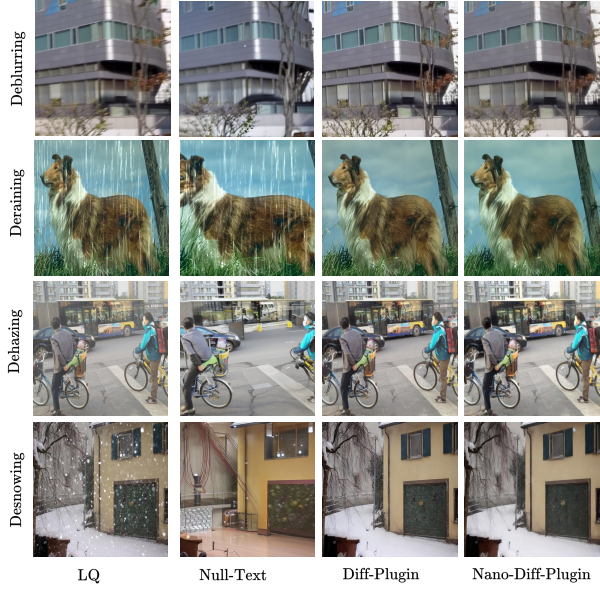


Figure 6. Qualitative comparisons of different methods for various restoration tasks. Please zoom in for a better view. Refer to Supplemental for more results.

Table 5. Quantitative comparison of the proposed Nano-Marigold with SOTA depth estimators on several zero-shot benchmarks. The best, second-best and third-best results are highlighted in red, blue, and green colors, respectively.

Method	NYU <sub>V2</sub> [37]		KITTI [11]	
	AbsRel $\downarrow$	$\delta 1 \uparrow$	AbsRel $\downarrow$	$\delta 1 \uparrow$
MiDAS [31]	11.1	88.5	23.6	63.0
LeRes [51]	9.0	91.6	14.9	78.4
Omnidata [9]	7.4	94.5	14.9	83.5
HDN [56]	6.9	94.8	11.5	86.7
DPT [32]	9.8	90.3	10.0	90.1
Marigold [17]	5.5	96.4	9.9	91.6
Nano-Marigold	7.2	94.6	11.8	86.3

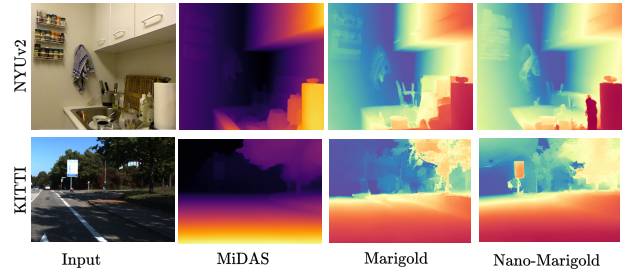


Figure 7. Qualitative comparison of various depth estimation methods across different datasets.

Nano-Diff-Plugin across four challenging low-level vision tasks.

Table 3 demonstrates that the proposed Nano-DiffBIR achieves competitive performance in terms of IQA metrics and restores identity as indicated by lower LMD score. Visual comparisons in Figure 5 reveal that the proposed approach effectively preserves facial identity while producing high-quality textures.

#### 4.6. Accelerating Marigold: Repurposing NanoSD for Monocular Depth Estimation

To harness the capabilities of a pretrained NanoSD model for monocular depth estimation, we incorporate it into Marigold—a latent diffusion framework tailored for depth prediction. The performance of Nano-Marigold in depth estimation is evaluated against alternative approaches in Table 5. The results demonstrate that our method achieves competitive results compared to prior work while maintaining robust generalization across diverse real-world scenarios. For qualitative analysis, Figure 7 presents a visual comparison. The results indicate that Nano-Marigold effectively captures both scene structure and fine-grained details with enhanced computational efficiency.

## 5. Conclusion

We introduced NanoSD, an edge-efficient diffusion model obtained by restructuring the SD 1.5 U-Net into a hardware-aware search space, distilling stage-wise block variants, and selecting compact backbones through multi-objective optimization. The selected model, NanoSD preserves the generative behavior of SD 1.5 across a range of low-level vision tasks while substantially reducing computational cost on edge.

## References

- [1] Eirikur Agustsson and Radu Timofte. Ntire 2017 challenge on single image super-resolution: Dataset and study. In *Proceedings of the IEEE conference on computer vision and pattern recognition workshops*, pages 126–135, 2017. 6, 8
- [2] Tim Brooks, Aleksander Holynski, and Alexei A Efros. Instructpix2pix: Learning to follow image editing instructions. In *Proceedings of the IEEE/CVF conference on computer vision and pattern recognition*, pages 18392–18402, 2023. 8
- [3] Yohann Cabon, Naila Murray, and Martin Humenberger. Virtual kitti 2. *arXiv preprint arXiv:2001.10773*, 2020. 6
- [4] Jianrui Cai, Hui Zeng, Hongwei Yong, Zisheng Cao, and Lei Zhang. Toward real-world single image super-resolution: A new benchmark and a new model. In *Proceedings of the IEEE/CVF international conference on computer vision*, pages 3086–3095, 2019. 6, 8
- [5] Bin Chen, Gehui Li, Rongyuan Wu, Xindong Zhang, Jie Chen, Jian Zhang, and Lei Zhang. Adversarial diffusion compression for real-world image super-resolution. In *Proceedings of the Computer Vision and Pattern Recognition Conference*, pages 28208–28220, 2025. 2, 6, 8
- [6] Jierun Chen, Dongting Hu, Xijie Huang, Huseyin Coskun, Arpit Sahni, Aarush Gupta, Anujraaj Goyal, Dishani Lahiri, Rajesh Singh, Yerlan Idelbayev, et al. Snapgen: Taming high-resolution text-to-image models for mobile devices with efficient architectures and training. In *Proceedings of the Computer Vision and Pattern Recognition Conference*, pages 7997–8008, 2025. 2
- [7] Keyan Ding, Kede Ma, Shiqi Wang, and Eero P Simoncelli. Image quality assessment: Unifying structure and texture similarity. *IEEE transactions on pattern analysis and machine intelligence*, 44(5):2567–2581, 2020. 6
- [8] Linwei Dong, Qingnan Fan, Yuhang Yu, Qi Zhang, Jinwei Chen, Yawei Luo, and Changqing Zou. Tinysr: Pruning diffusion for real-world image super-resolution. *arXiv preprint arXiv:2508.17434*, 2025. 2, 3, 6, 8
- [9] Ainaz Eftekhar, Alexander Sax, Jitendra Malik, and Amir Zamir. Omnidata: A scalable pipeline for making multi-task mid-level vision datasets from 3d scans. In *Proceedings of the IEEE/CVF International Conference on Computer Vision*, pages 10786–10796, 2021. 8
- [10] Patrick Esser, Sumith Kulal, Andreas Blattmann, Rahim Entezari, Jonas Müller, Harry Saini, Yam Levi, Dominik Lorenz, Axel Sauer, Frederic Boesel, et al. Scaling rectified flow transformers for high-resolution image synthesis. In *Forty-first international conference on machine learning*, 2024. 2
- [11] Andreas Geiger, Philip Lenz, and Raquel Urtasun. Are we ready for autonomous driving? the kitti vision benchmark suite. In *2012 IEEE conference on computer vision and pattern recognition*, pages 3354–3361. IEEE, 2012. 6, 8
- [12] Isma Hadji, Mehdi Noroozi, Victor Escorcia, Anestis Zaganidis, Brais Martinez, and Georgios Tzimiropoulos. Edgesd-sr: Low latency and parameter efficient on-device super-resolution with stable diffusion via bidirectional conditioning. In *Proceedings of the Computer Vision and Pattern Recognition Conference*, pages 12789–12798, 2025. 2, 3, 6, 8
- [13] Martin Heusel, Hubert Ramsauer, Thomas Unterthiner, Bernhard Nessler, and Sepp Hochreiter. Gans trained by a two time-scale update rule converge to a local nash equilibrium. *Advances in neural information processing systems*, 30, 2017. 6
- [14] Gary B Huang, Marwan Mattar, Tamara Berg, and Eric Learned-Miller. Labeled faces in the wild: A database forstudying face recognition in unconstrained environments. In *Workshop on faces in'Real-Life'Images: detection, alignment, and recognition*, 2008. 6, 10
- [15] Tero Karras, Timo Aila, Samuli Laine, and Jaakko Lehtinen. Progressive growing of gans for improved quality, stability, and variation. *arXiv preprint arXiv:1710.10196*, 2017. 6
- [16] Tero Karras, Samuli Laine, and Timo Aila. A style-based generator architecture for generative adversarial networks. In *Proceedings of the IEEE/CVF conference on computer vision and pattern recognition*, pages 4401–4410, 2019. 6
- [17] Bingxin Ke, Anton Obukhov, Shengyu Huang, Nando Metzger, Rodrigo Caye Daudt, and Konrad Schindler. Repurposing diffusion-based image generators for monocular depth estimation. In *Proceedings of the IEEE/CVF conference on computer vision and pattern recognition*, pages 9492–9502, 2024. 8
- [18] Junjie Ke, Qifei Wang, Yilin Wang, Peyman Milanfar, and Feng Yang. Musiq: Multi-scale image quality transformer. In *Proceedings of the IEEE/CVF international conference on computer vision*, pages 5148–5157, 2021. 6
- [19] Bo-Kyeong Kim, Hyoung-Kyu Song, Thibault Castells, and Shinkook Choi. On architectural compression of text-to-image diffusion models. 2023. 3, 5
- [20] Youngwan Lee, Kwanyong Park, Yoohim Cho, Yong-Ju Lee, and Sung Ju Hwang. Koala: Empirical lessons toward memory-efficient and fast diffusion models for text-to-image synthesis. *Advances in Neural Information Processing Systems*, 37:51597–51633, 2024. 3
- [21] Boyi Li, Wenqi Ren, Dengpan Fu, Dacheng Tao, Dan Feng, Wenjun Zeng, and Zhangyang Wang. Benchmarking single-image dehazing and beyond. *IEEE transactions on image processing*, 28(1):492–505, 2018. 6, 8
- [22] Boyi Li, Wenqi Ren, Dengpan Fu, Dacheng Tao, Dan Feng, Wenjun Zeng, and Zhangyang Wang. Benchmarking single-image dehazing and beyond. *IEEE transactions on image processing*, 28(1):492–505, 2018. 6

- [23] Yanyu Li, Huan Wang, Qing Jin, Ju Hu, Pavlo Chemerys, Yun Fu, Yanzhi Wang, Sergey Tulyakov, and Jian Ren. Snap-fusion: Text-to-image diffusion model on mobile devices within two seconds. *Advances in Neural Information Processing Systems*, 36:20662–20678, 2023. 2, 3
- [24] Yawei Li, Kai Zhang, Jingyun Liang, Jiezheng Cao, Ce Liu, Rui Gong, Yulun Zhang, Hao Tang, Yun Liu, Denis Deman-dolx, et al. Lsdir: A large scale dataset for image restoration. In *Proceedings of the IEEE/CVF Conference on Computer Vision and Pattern Recognition*, pages 1775–1787, 2023. 6
- [25] Xinqi Lin, Jingwen He, Ziyuan Chen, Zhaoyang Lyu, Bo Dai, Fanghua Yu, Yu Qiao, Wanli Ouyang, and Chao Dong. Diffbir: Toward blind image restoration with generative diffusion prior. In *European conference on computer vision*, pages 430–448. Springer, 2024. 2, 3, 6, 8, 10
- [26] Yuhao Liu, Zhanghan Ke, Fang Liu, Nanxuan Zhao, and Rynson WH Lau. Diff-plugin: Revitalizing details for diffusion-based low-level tasks. In *Proceedings of the IEEE/CVF Conference on Computer Vision and Pattern Recognition*, pages 4197–4208, 2024. 2, 3, 8
- [27] Yun-Fu Liu, Da-Wei Jaw, Shih-Chia Huang, and Jenq-Neng Hwang. Desnownet: Context-aware deep network for snow removal. *IEEE Transactions on Image Processing*, 27(6):3064–3073, 2018. 6, 8
- [28] Yun-Fu Liu, Da-Wei Jaw, Shih-Chia Huang, and Jenq-Neng Hwang. Desnownet: Context-aware deep network for snow removal. *IEEE Transactions on Image Processing*, 27(6):3064–3073, 2018. 6
- [29] Ron Mokady, Amir Hertz, Kfir Aberman, Yael Pritch, and Daniel Cohen-Or. Null-text inversion for editing real images using guided diffusion models. In *Proceedings of the IEEE/CVF conference on computer vision and pattern recognition*, pages 6038–6047, 2023. 8
- [30] Seungjun Nah, Tae Hyun Kim, and Kyoung Mu Lee. Deep multi-scale convolutional neural network for dynamic scene deblurring. In *Proceedings of the IEEE conference on computer vision and pattern recognition*, pages 3883–3891, 2017. 6
- [31] René Ranftl, Katrin Lasinger, David Hafner, Konrad Schindler, and Vladlen Koltun. Towards robust monocular depth estimation: Mixing datasets for zero-shot cross-dataset transfer. *IEEE transactions on pattern analysis and machine intelligence*, 44(3):1623–1637, 2020. 6, 8
- [32] René Ranftl, Alexey Bochkovskiy, and Vladlen Koltun. Vision transformers for dense prediction. In *Proceedings of the IEEE/CVF international conference on computer vision*, pages 12179–12188, 2021. 6, 8
- [33] Jaesung Rim, Haeyun Lee, Jucheol Won, and Sunghyun Cho. Real-world blur dataset for learning and benchmarking de-blurring algorithms. In *European conference on computer vision*, pages 184–201. Springer, 2020. 6, 8
- [34] Mike Roberts, Jason Ramapuram, Anurag Ranjan, Atulit Kumar, Miguel Angel Bautista, Nathan Paczan, Russ Webb, and Joshua M Susskind. Hypersim: A photorealistic synthetic dataset for holistic indoor scene understanding. In *Proceedings of the IEEE/CVF international conference on computer vision*, pages 10912–10922, 2021. 6
- [35] Robin Rombach, Andreas Blattmann, Dominik Lorenz, Patrick Esser, and Björn Ommer. High-resolution image synthesis with latent diffusion models. In *Proceedings of the IEEE/CVF conference on computer vision and pattern recognition*, pages 10684–10695, 2022. 2, 3, 8
- [36] Christoph Schuhmann, Romain Beaumont, Richard Vencu, Cade Gordon, Ross Wightman, Mehdi Cherti, Theo Coombes, Aarush Katta, Clayton Mullis, Mitchell Wortsman, et al. Laion-5b: An open large-scale dataset for training next generation image-text models. *Advances in neural information processing systems*, 35:25278–25294, 2022. 6
- [37] Nathan Silberman, Derek Hoiem, Pushmeet Kohli, and Rob Fergus. Indoor segmentation and support inference from rgbd images. In *European conference on computer vision*, pages 746–760. Springer, 2012. 6, 8
- [38] Jasper Snoek, Hugo Larochelle, and Ryan P. Adams. Practical bayesian optimization of machine learning algorithms. In *NeurIPS*, 2012. 5
- [39] Haoze Sun, Linfeng Jiang, Fan Li, Renjing Pei, Zhixin Wang, Yong Guo, Jiaqi Xu, Haoyu Chen, Jin Han, Fenglong Song, et al. Pocketsr: The super-resolution expert in your pocket mobiles. *arXiv preprint arXiv:2510.03012*, 2025. 2, 3, 6, 8
- [40] Jianyi Wang, Zongsheng Yue, Shangchen Zhou, Kelvin CK Chan, and Chen Change Loy. Exploiting diffusion prior for real-world image super-resolution. *International Journal of Computer Vision*, 132(12):5929–5949, 2024. 2, 8
- [41] Jingkai Wang, Jue Gong, Lin Zhang, Zheng Chen, Xing Liu, Hong Gu, Yutong Liu, Yulun Zhang, and Xiaokang Yang. Osdface: One-step diffusion model for face restoration. In *Proceedings of the Computer Vision and Pattern Recognition Conference*, pages 12626–12636, 2025. 2, 3, 6, 10
- [42] Tianyu Wang, Xin Yang, Ke Xu, Shaozhe Chen, Qiang Zhang, and Rynson WH Lau. Spatial attentive single-image deraining with a high quality real rain dataset. In *Proceedings of the IEEE/CVF conference on computer vision and pattern recognition*, pages 12270–12279, 2019. 6, 8
- [43] Xintao Wang, Yu Li, Honglun Zhang, and Ying Shan. Towards real-world blind face restoration with generative facial prior. In *Proceedings of the IEEE/CVF conference on computer vision and pattern recognition*, pages 9168–9178, 2021. 6, 10
- [44] Yufei Wang, Wenhan Yang, Xinyuan Chen, Yaohui Wang, Lanqing Guo, Lap-Pui Chau, Ziwei Liu, Yu Qiao, Alex C Kot, and Bihan Wen. Sinsr: diffusion-based image super-resolution in a single step. In *Proceedings of the IEEE/CVF conference on computer vision and pattern recognition*, pages 25796–25805, 2024. 2, 8
- [45] Zhou Wang, Alan C Bovik, Hamid R Sheikh, and Eero P Simoncelli. Image quality assessment: from error visibility to structural similarity. *IEEE transactions on image processing*, 13(4):600–612, 2004. 6
- [46] Pengxu Wei, Ziwei Xie, Hannan Lu, Zongyuan Zhan, Qixiang Ye, Wangmeng Zuo, and Liang Lin. Component divide-and-conquer for real-world image super-resolution. In *European conference on computer vision*, pages 101–117. Springer, 2020. 6, 8

- [47] Rongyuan Wu, Lingchen Sun, Zhiyuan Ma, and Lei Zhang. One-step effective diffusion network for real-world image super-resolution. *Advances in Neural Information Processing Systems*, 37:92529–92553, 2024. [2](#), [3](#), [8](#), [10](#)
- [48] Rongyuan Wu, Tao Yang, Lingchen Sun, Zhengqiang Zhang, Shuai Li, and Lei Zhang. Seesr: Towards semantics-aware real-world image super-resolution. In *Proceedings of the IEEE/CVF conference on computer vision and pattern recognition*, pages 25456–25467, 2024. [2](#), [8](#)
- [49] Peiqing Yang, Shangchen Zhou, Qingyi Tao, and Chen Change Loy. Pgdif: Guiding diffusion models for versatile face restoration via partial guidance. *Advances in Neural Information Processing Systems*, 36: 32194–32214, 2023. [6](#), [10](#)
- [50] Tao Yang, Rongyuan Wu, Peiran Ren, Xuansong Xie, and Lei Zhang. Pixel-aware stable diffusion for realistic image super-resolution and personalized stylization. In *European conference on computer vision*, pages 74–91. Springer, 2024. [2](#)
- [51] Wei Yin, Jianming Zhang, Oliver Wang, Simon Niklaus, Long Mai, Simon Chen, and Chunhua Shen. Learning to recover 3d scene shape from a single image. In *Proceedings of the IEEE/CVF conference on computer vision and pattern recognition*, pages 204–213, 2021. [8](#)
- [52] Zongsheng Yue and Chen Change Loy. Difface: Blind face restoration with diffused error contraction. *IEEE Transactions on Pattern Analysis and Machine Intelligence*, 2024. [6](#), [10](#)
- [53] Zongsheng Yue, Jianyi Wang, and Chen Change Loy. Resshift: Efficient diffusion model for image super-resolution by residual shifting. *Advances in Neural Information Processing Systems*, 36:13294–13307, 2023. [2](#), [8](#)
- [54] Syed Waqas Zamir, Aditya Arora, Salman Khan, Munawar Hayat, Fahad Shahbaz Khan, Ming-Hsuan Yang, and Ling Shao. Multi-stage progressive image restoration. In *Proceedings of the IEEE/CVF conference on computer vision and pattern recognition*, pages 14821–14831, 2021. [6](#)
- [55] Aiping Zhang, Zongsheng Yue, Renjing Pei, Wenqi Ren, and Xiaochun Cao. Degradation-guided one-step image super-resolution with diffusion priors. *arXiv preprint arXiv:2409.17058*, 2024. [2](#), [3](#), [8](#)
- [56] Chi Zhang, Wei Yin, Billzb Wang, Gang Yu, Bin Fu, and Chunhua Shen. Hierarchical normalization for robust monocular depth estimation. *Advances in Neural Information Processing Systems*, 35:14128–14139, 2022. [8](#)
- [57] Lin Zhang, Lei Zhang, and Alan C Bovik. A feature-enriched completely blind image quality evaluator. *IEEE Transactions on Image Processing*, 24(8):2579–2591, 2015. [6](#)
- [58] Lvmin Zhang, Anyi Rao, and Maneesh Agrawala. Adding conditional control to text-to-image diffusion models. In *Proceedings of the IEEE/CVF international conference on computer vision*, pages 3836–3847, 2023. [2](#), [8](#)
- [59] Richard Zhang, Phillip Isola, Alexei A Efros, Eli Shechtman, and Oliver Wang. The unreasonable effectiveness of deep features as a perceptual metric. In *Proceedings of the IEEE conference on computer vision and pattern recognition*, pages 586–595, 2018. [6](#), [1](#)
- [60] Yang Zhao, Yanwu Xu, Zhisheng Xiao, Haolin Jia, and Tingbo Hou. Mobiledonfusion: Instant text-to-image generation on mobile devices. In *European Conference on Computer Vision*, pages 225–242. Springer, 2024. [2](#)
- [61] Shangchen Zhou, Kelvin Chan, Chongyi Li, and Chen Change Loy. Towards robust blind face restoration with codebook lookup transformer. *Advances in Neural Information Processing Systems*, 35:30599–30611, 2022. [2](#), [6](#), [10](#)
- [62] Yuanzhi Zhu, Kai Zhang, Jingyun Liang, Jiezhang Cao, Bihan Wen, Radu Timofte, and Luc Van Gool. Denoising diffusion models for plug-and-play image restoration. In *Proceedings of the IEEE/CVF conference on computer vision and pattern recognition*, pages 1219–1229, 2023. [2](#)

# NanoSD: Edge Efficient Foundation Model for Real Time Image Restoration

## Supplementary Material

### 6. Analysis of Generative Prior in NanoSD

A central claim of this work is that NanoSD retains the generative prior inherited from the original SD 1.5 backbone, even after undergoing distillation and downstream task adaptation. To validate this claim, we perform comprehensive qualitative and quantitative analyses, comparing NanoSD with both SD 1.5 and a computationally equivalent UNet-based restoration baseline.

#### 6.1. Exploring the Latent Space Manifold

To evaluate whether NanoSD preserves the structured latent manifold inherent to SD 1.5, we perform latent-space interpolation between two Gaussian noise samples. As demonstrated in Fig. 8, both SD 1.5 and NanoSD exhibit smooth and semantically consistent transitions along the interpolation path, maintaining scene layout and object semantics. This behavior suggests that NanoSD successfully retains the high-level generative structure of the original diffusion model.

#### 6.2. Exploring Embedding-Based Similarity and Perceptual Consistency

To quantitatively assess prior preservation, we measure embedding-based similarities using CLIP encoders. If NanoSD successfully retains the generative prior of SD 1.5, its outputs should maintain proximity to the distribution generated by the original SD 1.5 model. As evidenced in Table 6, NanoSD demonstrates significantly higher similarity to SD 1.5 compared to the U-Net baseline, while approaching the self-consistency of SD 1.5 evaluated across independent sampling runs. These results indicate that NanoSD effectively preserves the generative manifold of the original SD 1.5 model.

We further assess perceptual fidelity using the Learned Perceptual Image Patch Similarity (LPIPS) [59] metric for image super-resolution. As shown in Table 6, NanoSD achieves a substantially lower perceptual distance to SD 1.5 compared to the UNet baseline. Crucially, the LPIPS difference between NanoSD and SD 1.5 is only marginally larger than the variation observed between different SD 1.5 outputs generated with distinct random seeds. This narrow margin demonstrates that NanoSD maintains strong alignment with the teacher model’s output distribution despite the distillation process.

### 7. Real-time Image Restoration using NanoSD

#### 7.1. Mobile ISP for Image Restoration

We address the significant challenge of developing a foundation model capable of preserving generative priors while operating efficiently on resource-constrained edge devices. Deploying such models on mobile platforms presents multiple practical obstacles, including large model sizes and high inference latency. These challenges are particularly pronounced for restoration tasks, which typically require processing high-resolution images through multiple model runs. For instance, modern smartphones often capture images at  $4K \times 3K$  resolution, whereas diffusion-based models like StableSR typically generate  $512 \times 512$  patches per forward pass. This discrepancy necessitates tile-based processing, where a  $1000 \times 750$  low-quality input image is divided into  $128 \times 128$  patches with 25% overlap, resulting in 88 patches that must be processed sequentially as shown in Fig 9. Each tile undergoes one or more diffusion steps, substantially increasing computational overhead and runtime.

#### 7.2. Limitations of SD 1.5 for Edge Deployment

While diffusion models such as SD 1.5 offer strong generative priors, their computational and memory demands make them fundamentally unsuitable for resource-constrained devices. SD 1.5 contains approximately 829 million parameters, corresponding to about 3.3 GB of raw model weights in Full precision. Even with INT8 quantization, the footprint remains roughly 0.8 GB, exceeding the memory budgets of mobile NPUs, which must also accommodate activation buffers, intermediate tensors, runtime libraries, and system services. This alone renders SD 1.5 impractical for on-device deployment.

In practice, the situation is even more restrictive. Attempts to deploy SD 1.5 on commercial mobile chipsets failed to generate executable binaries for both Qualcomm NPUs (Android) and the Apple Neural Engine (iOS) when using FP32, INT16, or INT8 precision. Even aggressive INT4 quantization—despite its substantial accuracy degradation—yielded a model with an average latency of 116 ms per tile on the Qualcomm Snapdragon SM8750 NPU.

Recalling the tile-based pipeline described previously, a  $1000 \times 750$  input image requires 88 tiles at  $128 \times 128$  resolution. Thus, the end-to-end runtime of SD 1.5 becomes 10.2 seconds ( 88 tiles x 116 ms/tile). This latency corresponds to a *single* diffusion step, whereas restoration pipelines typically require multiple steps or sequential sub-networks (e.g., face refinement or iterative enhancement). Such runtimes are incompatible with real-time or interac-

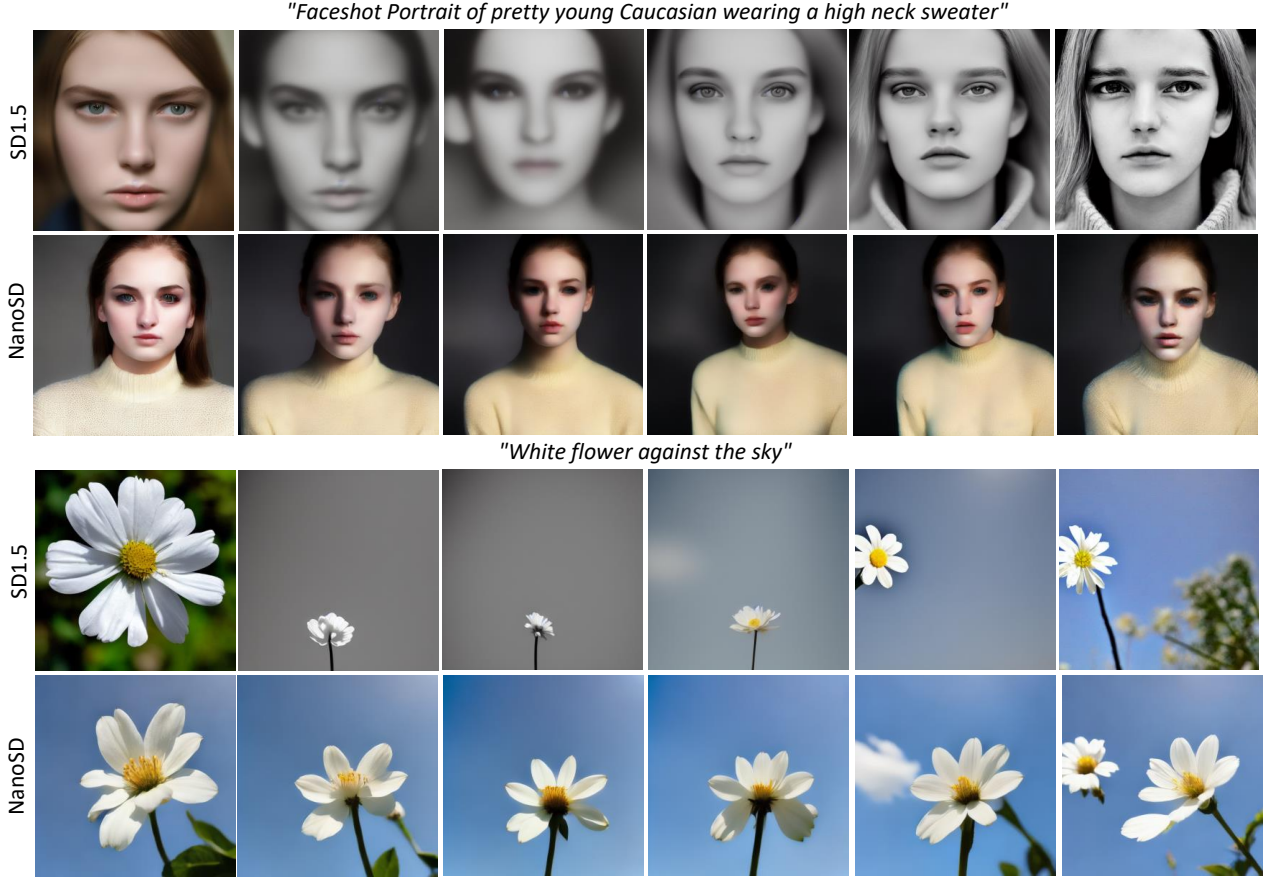


Figure 8. Latent-space interpolation between two random seeds for both SD 1.5 and NanoSD. The results demonstrate smooth transitions in the generated outputs along the interpolation trajectories for both models. This observation confirms that NanoSD preserves a well-structured latent manifold, maintaining consistency with the generative prior learned by SD 1.5.

Table 6. Perceptual distance measured using LPIPS and embedding-space similarity via CLIP embeddings between SD 1.5 outputs and other competitive models. Our results demonstrate that NanoSD maintains significantly closer proximity to SD 1.5 than the regression-based U-Net baseline. This quantitative evidence indicates robust preservation of SD 1.5’s generative prior in the distilled NanoSD model.

Model Pair	LPIPS $\downarrow$	Embedding Cosine Similarity $\uparrow$
SD 1.5 vs SD 1.5 (two random runs)	0.48	0.89
NanoSD vs SD 1.5	0.57	0.84
UNet-Baseline vs SD 1.5	1.92	0.41

tive workloads. Together, these memory, compilation, and runtime constraints demonstrate why SD 1.5 is unsuitable for deployment on modern mobile devices and motivate the need for an edge-aware redesign.

### 7.3. Hardware-Aware Network Surgery

To bridge this gap, we perform a principled hardware-aware decomposition of the SD 1.5 U-Net. Rather than applying uniform pruning or parameter-centric compression, we restructure the network at the block level through *network*

*surgery*. Specifically, we identify alternative block configurations—such as residual-only, reduced-attention, or hybrid arrangements—that preserve the input–output tensor shapes of the original SD 1.5 blocks. These alternatives are then individually profiled on the Qualcomm SM8750 NPU, enabling us to measure the true hardware latency of each candidate block.

This profiling reveals substantial variation in runtime among shape-compatible alternatives, with several variants offering 3–8 $\times$  lower latency despite comparable parameter

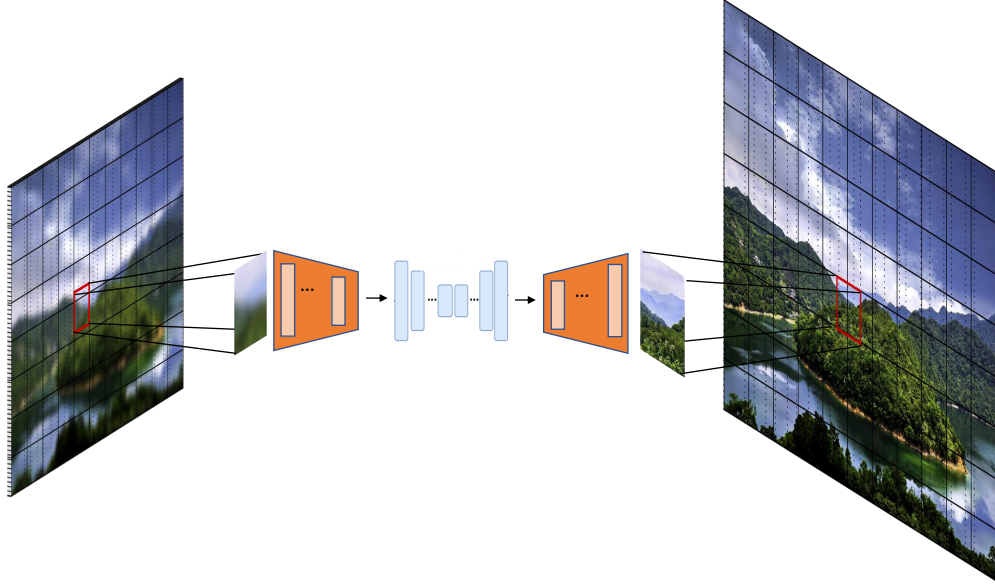


Figure 9. NanoSD employs a tiled inference strategy to enable high-resolution image restoration on edge computing platforms. The processing pipeline begins by partitioning a  $1000 \times 750$  input image into  $128 \times 128$  overlapping tiles (25% overlap), generating 88 total tiles. Each tile undergoes independent processing through the NanoSD model before being reassembled into a final 4K resolution output. This tile-based approach achieves two critical objectives: (1) maintaining perceptual consistency across the reconstructed image, and (2) meeting the computational constraints of mobile processors for real-time operation. The method effectively balances restoration quality with the practical requirements of edge deployment.

Table 7. Latency profiling of 30 surrogate U-Net blocks on Qualcomm SM8750 NPU (Samsung S25 Ultra). We report the measured per-block latency for all hardware-aware alternatives generated via network surgery. Although all variants preserve tensor shapes and remain accuracy-compatible after feature wise distillation, they exhibit substantial diversity in hardware cost, with several alternatives achieving 3-8 $\times$  lower latency than the original SD 1.5 blocks. These measurements form the basis of the hardware-aware search space used in our Pareto optimization.

Encoder 1		Encoder 2		Encoder 3	
Alternative	Latency (ms)	Alternative	Latency (ms)	Alternative	Latency (ms)
R	3	R	1.79	R	1.1
RA	12.5	RA	3.7	RA	1.46
RR	3.5	RR	3	RR	1.2
Decoder 1		Decoder 2		Decoder 3	
Alternative	Latency (ms)	Alternative	Latency (ms)	Alternative	Latency (ms)
R	1.7	R	2.07	R	1.3
RA	16.3	RA	5.8	RA	3.4
RR	3.1	RR	3.17	RR	2.3
RRA	17.3	RRA	6.8	RRA	4.2
RAR	17.7	RAR	7.5	RAR	4.5
RRRA	19	RRRA	8.8	RRRA	5.5
RARR	19.1	RARR	7.9	RARR	5.2
RARA	39	RARA	12.8	RARA	5.5

counts. Table 7 lists all 30 surrogate blocks and their measured latencies on the SM8750 NPU in full precision. Such profiling enables us to embed hardware cost directly into the design space, avoiding reliance on FLOPs or parameter count, which correlate poorly with real-world latency due

to tensor-movement and memory-access bottlenecks.

While hardware profiling identifies efficient block candidates, directly substituting them into the U-Net would disrupt SD 1.5’s generative prior. To preserve fidelity, we apply *Feature-wise Generative Distillation* (FwGD) to every can-

Table 8. Cross-platform latency analysis of NanoSD family on the Apple A17 Pro Neural Engine (iOS). We evaluate all U-Net candidates from the NanoSD Pareto set—originally optimized using Qualcomm SM8750 latency data—on the Apple ANE without modification. The relative latency ordering and efficiency trends mirror those observed on SM8750, confirming that the proposed hardware-aware search produces architectures that generalize across accelerators. This consistency demonstrates the hardware-agnostic nature of our method and highlights the limitations of FLOP- or parameter-centric compression for predicting real-world edge performance.

Model	Latency (ms)	
	Qualcomm	Apple
<b>TinySD</b>	74	192
<b>Hand-tuned</b>	53	133
<b>NanoSD 1</b>	41	82
<b>NanoSD 2</b>	27	38
<b>NanoSD 3</b>	24	34
<b>NanoSD 4</b>	20	31
<b>NanoSD 5</b>	12	20
<b>NanoSD 6</b>	28	68
<b>NanoSD 7</b>	27	66

didate block: each surrogate is trained to match the output distribution of its corresponding SD 1.5 teacher block under identical inputs. The structural compatibility between the base block and each hardware-aware alternative ensures the path for knowledge transfer to compact, local modules, enabling massively parallel and computationally lightweight training.

FwGD provides two essential benefits:

- **Accuracy preservation.** Each block independently inherits SD 1.5’s generative behavior, allowing arbitrary combinations of surrogates to form valid U-Nets without catastrophic feature drift.
- **Search-space validity.** By distilling all block variants, the search space contains only architectures that are simultaneously hardware-efficient and accuracy-sufficient.

Together, hardware-aware network surgery and FwGD yield a search space that is structurally valid, hardware-aligned, and generative-prior-preserving—properties crucial for downstream optimization.

#### 7.4. Why Hardware Awareness Is Essential?

If the search space were constructed solely using parameter reduction, FLOPs minimization, or uniform pruning, the resulting architectures would not necessarily yield improvements in *true* edge latency. In hierarchical U-Nets, inner blocks operate at low spatial resolutions, so reducing their parameters has minimal effect on runtime. Conversely, even small modifications to early, high-resolution stages significantly reduce latency due to the cost of propagating large

activation maps. This mismatch between compute-centric metrics and latency-critical behavior explains why SD 1.5 cannot simply be “compressed” into an edge model.

By profiling block alternatives directly on NPU hardware, our method ensures that latency-critical regions receive appropriate structural simplifications. Combined with FwGD, this yields a hardware-aware and accuracy-aligned search space from which Bayesian optimization extracts Pareto-optimal U-Nets, ultimately producing the NanoSD architecture. This synergy between hardware profiling, network surgery, and block-level distillation fundamentally differentiates our method from FLOP-centric or parameter-centric reduction techniques.

#### 7.5. Generic Nature of the Proposal

To assess the generality of our approach, we replicated the hardware profiling procedure on a second, architecturally distinct platform: the Apple A17 Pro Neural Engine (ANE) on iOS. Although the network surgery and Pareto optimization were performed using latency measurements from the Qualcomm SM8750 NPU on the Samsung S25 Ultra, we evaluated the resulting NanoSD family on the ANE without modification. As shown in Table 8, the latency trends on the ANE closely mirror those observed on the SM8750: NanoSD variants consistently outperform the SD 1.5 baseline and manually designed alternatives despite differences in compiler stacks, operator scheduling, and memory hierarchies across the two platforms. This consistency demonstrates that the proposed method is inherently hardware-agnostic: rather than tailoring a model to a single device, it constructs a search space aware of device characteristics while remaining compatible with any backend NPU. These results reinforce that FLOPs and parameter count alone are insufficient predictors of on-device performance, and that explicit hardware-aware decomposition is essential for designing diffusion models suitable for diverse edge environments.

#### 7.6. Edge efficiency of NanoSD

We conduct a systematic evaluation of NanoSD’s computational efficiency to assess its viability for edge deployment in high-resolution image restoration applications. Our quantitative analysis reveals that NanoSD achieves inference latencies compatible with real-time operational requirements on mobile platforms. Specifically, the model processes a  $128 \times 128$  input tile to produce a  $512 \times 512$  output in approximately 20 ms when running on mobile neural processing units (NPUs). For processing  $4000 \times 3000$  image, the total end-to-end latency measures of about 1.8 seconds on equivalent hardware, accounting for all 88 required tile evaluations. These empirical results provide compelling evidence that diffusion-based restoration can be effectively implemented on-device, satisfying the stringent computa-

tional constraints of mobile platforms while eliminating the need for cloud-based processing.

## 8. Bayesian Optimization with EHVI

We cast the selection of an efficient U-Net backbone from the discrete hardware-aware search space as a multi-objective black-box optimization problem. Let  $\mathcal{Z}$  denote the discrete set of feasible architectures induced by stage-wise block choices. For any architecture  $\mathbf{z} \in \mathcal{Z}$  we evaluate two primary objectives:

$$f_{\text{FID}}(\mathbf{z}) = \text{FID}\left(\hat{X}(\mathbf{z}), X_{\text{SD1.5}}\right), \quad (7)$$

$$f_{\text{param}}(\mathbf{z}), \quad f_{\text{latency}}(\mathbf{z}). \quad (8)$$

where  $f_{\text{FID}}$ , the first objective ( $f_1$ ), is the teacher-aligned FID measured against SD 1.5 outputs, the second objective ( $f_2$ ) is either  $f_{\text{latency}}$ , the on-device latency or  $f_{\text{param}}$ , the parameter count, depending on the search iteration.

Direct optimization over  $\mathcal{Z}$  is expensive because each evaluation of  $f_1$  requires many diffusion samples and FID computation. We therefore employ Bayesian Optimization (BO) with Expected Hypervolume Improvement (EHVI) [38] as the acquisition function to efficiently explore  $\mathcal{Z}$ . To handle the discrete nature of  $\mathcal{Z}$  we adopt a two-step relaxed-and-project approach: (1) represent architecture choices by a continuous proxy  $\mathbf{x} \in [0, 1]^d$  (here  $d$  is the number of design dimensions), (2) map  $\mathbf{x}$  to the nearest feasible discrete architecture via a deterministic projection  $\phi : [0, 1]^d \rightarrow \mathcal{Z}$ .

The BO loop proceeds as follows. We fit independent Gaussian Process (GP) surrogates to the observed values of each objective over previously evaluated architectures. EHVI is computed with respect to the current Pareto set and used to propose the next continuous candidate  $\mathbf{x}^*$ . The projection  $\mathbf{z}^* = \phi(\mathbf{x}^*)$  yields a discrete architecture which is assembled from the distilled surrogate blocks and then evaluated to obtain  $(f_1(\mathbf{z}^*), f_2(\mathbf{z}^*))$ . The GP models are updated and the Pareto set is expanded accordingly. Iteration continues until a predefined budget of evaluations is exhausted, resulting the final Pareto set as shown in Figure 2 in the main paper.

## 9. VAE Distillation

Our objective is to obtain a fully edge-optimized latent diffusion model by compressing all major components of Stable Diffusion 1.5—the U-Net, VAE encoder, and VAE decoder—while preserving compatibility with the teacher model’s generative behavior. Starting from a pretrained SD 1.5 pipeline, we first distill the U-Net, then distill the VAE encoder and decoder with the U-Net frozen, and finally refine the assembled pipeline for end-to-end consistency.

Table 9 provides an overview and includes the distilled architectures of both the encoder and decoder. The proposed student VAE is highly parameter- and latency-efficient: its encoder and decoder contain only  $\sim 2$  M and  $\sim 1.3$  M parameters (10 ms and 8 ms FP16 latency, respectively), compared to the much larger SD1.5 VAE. This reduction is achieved by using fixed-width (64-channel) Tiny ResNet blocks and shallow lightweight up/downsampling stages instead of the widening  $64 \rightarrow 128 \rightarrow 256 \rightarrow 512$  ResNet blocks used in the teacher.

### 9.1. Preliminaries

Let  $E_t$ ,  $D_t$ , and  $U_t$  denote the teacher VAE encoder, VAE decoder, and diffusion U-Net. The encoder outputs posterior parameters

$$(\mu_t(x), \log \sigma_t^2(x)) = E_t(x). \quad (9)$$

Latent sampling follows

$$z_t = \mu_t(x) + \sigma_t(x) \odot \epsilon, \quad \epsilon \sim \mathcal{N}(0, I). \quad (10)$$

Scaled latents are fed into the U-Net:

$$\tilde{z}_t = \alpha z_t, \quad \alpha = 0.18215. \quad (11)$$

The U-Net predicts noise conditioned on time step  $t$  and text embedding  $c$ :

$$\epsilon_t = U_t(\tilde{z}_t, t, c). \quad (12)$$

Our goal is to obtain student modules  $E_s$ ,  $D_s$ , and  $U_s$  such that the resulting pipeline remains distributionally aligned with the teacher.

### 9.2. Stage I: U-Net Distillation

The student U-Net  $U_s$  is trained via the proposed formulation (see Figure 2 in main paper) for edge efficiency, resulting in the NanoSD U-Net. After this stage,  $U_s$  is frozen for the remainder of training.

### 9.3. Stage II: Encoder Distillation

The student encoder outputs

$$(\mu_s(x), \log \sigma_s^2(x)) = E_s(x), \quad (13)$$

and is trained to match the teacher encoder via

$$\mathcal{L}_{\text{latent}} = \|\mu_t(x) - \mu_s(x)\|_2^2 + \|\sigma_t(x) - \sigma_s(x)\|_2^2. \quad (14)$$

A weak KL regularization term is included:

$$\mathcal{L}_{\text{KL}} = D_{\text{KL}}(q_s(z | x) \| \mathcal{N}(0, I)). \quad (15)$$

The encoder objective is:

$$\mathcal{L}_E = \mathcal{L}_{\text{latent}} + \beta \mathcal{L}_{\text{KL}}, \quad \beta \in [10^{-6}, 10^{-4}]. \quad (16)$$

Table 9. Architectural comparison of the Teacher VAE (SD 1.5) and the proposed Student VAE. Both models are shown using a unified notation with identical spatial dimensions. Only architectural differences are listed. ResNetBlockTiny refers to a lightweight residual block that preserves the Conv–Norm–Activation–Conv pattern of a standard ResNet block but replaces the full  $3 \times 3$  convolutions with parameter-efficient variants (e.g. depthwise–separable convs) operating at a fixed 64-channel width. This makes each block an order of magnitude smaller than the full ResNet blocks in the SD 1.5 encoder.

Teacher VAE (SD 1.5)	Student VAE (Proposed)
<b>Encoder Architecture (Input: <math>3 \times H \times W</math>)</b>	
<b>Stem:</b> Conv(3→64), ResNetBlock ×2. Resolution preserved.	<b>Stem:</b> Conv(3→64), <b>ResNetBlockTiny ×1</b> . Resolution preserved.
<b>Down Block 1:</b> ResNetBlock ×2 @ 64 ch, stride-2 Conv → $H/2 \times W/2$ .	<b>Down Block 1:</b> <b>ResNetBlockTiny ×3</b> @ 64 ch, stride-2 Conv → $H/2 \times W/2$ .
<b>Down Block 2:</b> ResNetBlock ×2 @ 128 ch, stride-2 Conv → $H/4 \times W/4$ .	<b>Down Block 2:</b> <b>ResNetBlockTiny ×3</b> @ 64 ch, stride-2 Conv → $H/4 \times W/4$ .
<b>Down Block 3:</b> ResNetBlock ×2 @ 256 ch, stride-2 Conv → $H/8 \times W/8$ .	<b>Down Block 3:</b> <b>ResNetBlockTiny ×3</b> @ 64 ch, stride-2 Conv → $H/8 \times W/8$ .
<b>Middle/Bottleneck:</b> ResNetBlock ×2 @ 512 ch.	<b>Middle/Bottleneck:</b> (no dedicated bottleneck; final stage already at 64 ch).
<b>Output projection:</b> Conv→8 ch.	<b>Output projection:</b> Conv→4 ch.
<b>Decoder Architecture (Input: <math>z \in \mathbb{R}^{4 \times (H/8) \times (W/8)}</math>)</b>	
<b>Stem:</b> Conv(4→512).	<b>Stem:</b> Conv(4→64).
<b>Middle/Bottleneck:</b> ResNetBlock ×2 @ 512 ch.	<b>Middle/Bottleneck:</b> ResNetBlock ×1 @ 64 ch.
<b>Up Block 1:</b> Upsample×2, ResNetBlock ×2 (512→256) → $H/4 \times W/4$ .	<b>Up Block 1:</b> ResNetBlock ×2 @ 64 ch, Upsample×2 → $H/4 \times W/4$ .
<b>Up Block 2:</b> Upsample×2, ResNetBlock ×2 (256→128) → $H/2 \times W/2$ .	<b>Up Block 2:</b> ResNetBlock (→128 ch), Upsample×2 → $H/2 \times W/2$ .
<b>Up Block 3:</b> Upsample×2, ResNetBlock ×2 (128→64) → $H \times W$ .	<b>Up Block 3:</b> ResNetBlock @ 128 ch, Upsample×2 → $H \times W$ .
<b>Final projection:</b> Conv(64→3).	<b>Final projection:</b> Conv(128→3).

#### 9.4. Stage III: Decoder Distillation

Given teacher latents  $z_t$ , the teacher and student reconstructions are:

$$\hat{x}_t = D_t(z_t), \quad \hat{x}_s = D_s(z_t). \quad (17)$$

Teacher-guided reconstruction is enforced via

$$\mathcal{L}_{\text{recon}} = \|\hat{x}_t - \hat{x}_s\|_1. \quad (18)$$

A perceptual loss aligns higher-level features:

$$\mathcal{L}_{\text{perc}} = \|\phi(\hat{x}_t) - \phi(\hat{x}_s)\|_2^2. \quad (19)$$

To ensure decoder robustness to student latents  $z_s$ , we include

$$\mathcal{L}_{\text{AE}} = \|x - D_s(z_s)\|_1. \quad (20)$$

The decoder objective is thus

$$\mathcal{L}_D = \mathcal{L}_{\text{recon}} + \lambda_{\text{perc}} \mathcal{L}_{\text{perc}} + \lambda_{\text{AE}} \mathcal{L}_{\text{AE}}. \quad (21)$$

#### 9.5. Stage IV: Joint VAE Refinement

Once  $E_s$  and  $D_s$  are individually trained, we jointly refine them using

$$\mathcal{L}_{\text{VAE}} = \lambda_1 \|x - D_s(E_s(x))\|_1 + \lambda_2 \mathcal{L}_{\text{perc}} + \lambda_3 D_{\text{KL}}(q_s \| \mathcal{N}(0, I)). \quad (22)$$

#### 9.6. Stage V: End-to-End Diffusion Alignment

To compensate for latent shift introduced by VAE compression, we lightly fine-tune  $U_s$  while keeping  $E_s$  and  $D_s$  frozen:

$$\mathcal{L}_{\text{align}} = \|U_s(\alpha z_s + \sigma_t \epsilon, t, c) - U_t(\alpha z_t + \sigma_t \epsilon, t, c)\|_2^2. \quad (23)$$

This multi-stage procedure yields a compact, edge-efficient latent diffusion model that preserves the generative behavior of SD 1.5 while enabling practical on-device deployment.

## 10. Implementation Details

**Hardware for Latency Profiling.** All hardware-aware latency measurements were performed on a Qualcomm Snapdragon SM8750 NPU deployed on a Samsung Galaxy S25 Ultra. Each of the 30 block alternatives was compiled using Qualcomm SNPE with INT8 weights and FP16 activations, and latency was averaged over 256 runs after discarding the first 20 warm-up iterations. To assess generality across heterogeneous hardware, the final NanoSD U-Net family was also profiled on the Apple A17 Pro Neural Engine using CoreML Tools on iOS 17, where a consistent latency ranking was observed (Table 8).

**Dataset for Distillation.** Feature-wise Generative Distillation, VAE distillation, and end-to-end alignment were all conducted using a representative subset of approximately 1 million image-text pairs sampled from a LAION-style corpus. This subset was stratified across prompt categories and image types to ensure coverage equivalent to the teacher model’s operating distribution. A held-out validation subset of 50,000 samples was used for early stopping and monitoring drift.

**Feature-wise Generative Distillation of 30 Surrogates.** Each of the 30 U-Net surrogate blocks was distilled independently against the corresponding SD 1.5 teacher block. We used AdamW (learning rate  $1 \times 10^{-4}$ , weight decay 0.01), batch size 128, cosine decay schedule with 2k warmup steps, and 15k–40k training iterations depending on block complexity. The total compute budget for all 30 surrogates was approximately 360 A100 GPU-hours. Parallel training across multiple GPUs allowed all surrogates to be distilled simultaneously.

**Bayesian Optimization Configuration.** Bayesian optimization was applied separately for the two bi-objective settings: (i) taFID vs. edge latency, and (ii) taFID vs. parameter count. We used a 6-dimensional continuous relaxation of the discrete search space, projected to feasible architectures via a deterministic thresholding map. Independent Gaussian Processes with Matérn-5/2 kernels were fitted to both objectives. The acquisition function was Expected Hypervolume Improvement (EHVI). We used 15 random initial samples and 120 BO iterations per run, and performed 5 independent runs with different seeds. The total compute cost for BO evaluation-dominated by taFID computation was approximately 100 A100 GPU-hours.

**VAE Encoder and Decoder Distillation.** After selecting the NanoSD U-Net, we distilled the VAE encoder and decoder using the same 1M-sample dataset. The encoder was trained with AdamW (learning rate  $5 \times 10^{-5}$ , batch size 64)

for 40k iterations, minimizing latent-matching and KL regularization losses with  $\beta \in [10^{-6}, 10^{-4}]$ . The decoder was trained for 80k–120k iterations with AdamW (learning rate  $1 \times 10^{-4}$ ), using reconstruction, perceptual, and autoencoding consistency losses. Combined encoder+decoder distillation required approximately 220 A100 GPU-hours.

**End-to-End Diffusion Alignment.** To compensate for the mild latent shift introduced by VAE compression, we performed a lightweight end-to-end noise-prediction alignment stage. The NanoSD U-Net was fine-tuned with a small learning rate ( $1 \times 10^{-6}$ ) for 20k–40k steps, with the VAE frozen. We used batch size 32, random timesteps, and kept the text encoder frozen. This stage required an additional 70 A100 GPU-hours.

**Total Compute.** Across all stages (FwGD, BO evaluations, VAE distillation, and T2I end-to-end alignment), the complete NanoSD pipeline required approximately 750 A100 GPU-hours—substantially lower than training or distilling a full SD 1.5 model, while enabling hardware-aware optimization tailored to edge devices.

## 11. Experimental Results

We present a detailed experimental and ablation analysis of various low-level vision tasks using the proposed NanoSD.

### 11.1. Ablation on Removing E4–Mid–D4 Blocks.

Prior work has shown that the highest-resolution stages of the U-Net dominate per-layer computational cost, whereas the lowest-resolution stages contribute disproportionately to the memory footprint with a limited effect on perceptual quality. Motivated by this observation, our default search space removes the encoder-4, mid, and decoder-4 blocks (E4–Mid–D4). To validate this choice, we reintroduced these three blocks (configured as E4 :  $R \rightarrow Mid : RAR \rightarrow D4 : RR$ ) into one of our baseline models, NanoSD 1 (see Table 1 of the main paper). The original model has a latency of 41 ms and 309 M parameters. After adding E4–Mid–D4, the parameter count increases substantially to 565 M, while latency increases only marginally to 46 ms due to the small spatial resolutions processed by these blocks.

We compare the pre-finetuning image quality of the two variants in Figure 10. Despite the large increase in parameters and memory footprint, the improvement in visual quality is negligible. This confirms that the cost of including E4–Mid–D4 is not justified for edge-efficient models, and supports our decision to exclude these blocks from the search space.

Table 10. Quantitative comparison of different methods on DIV-2K Val [1]to dataset. The best, second-best and third-best results are highlighted in red, blue, and green colors, respectively.

Method	PSNR↑	SSIM↑	LPIPS↓	FID↓	NIQE↓	MUSIQ↑	Steps	MACs (G)	Para. (M)
StableSR [40]	23.26	0.572	0.311	24.44	4.75	65.92	200	79940	1410
DiffBIR [25]	23.64	0.564	0.352	30.72	4.70	65.81	50	24234	1717
SeeSR [48]	23.68	0.604	0.319	25.90	4.81	68.67	50	65857	2524
ResShift [53]	24.65	0.618	0.334	36.11	6.82	61.09	15	5491	119
SinSR [44]	24.41	0.601	0.324	35.57	6.02	62.82	1	2649	119
OSEDiff [47]	23.72	0.610	0.294	26.32	4.71	67.97	1	2265	1775
S3Diff [55]	23.52	0.594	0.258	19.66	4.74	68.01	1	2621	1327
TinySR [8]	-	0.572	0.279	22.94	4.15	69.90	1	427	341
Edge-SD-SR [12]	24.10	0.617	0.249	25.37	-	69.58	1	-	169
PocketSR [39]	23.85	0.601	0.280	25.25	4.415	66.38	1	225	146
AdcSR [5]	23.74	0.601	0.285	25.52	4.36	68.00	1	496	456
Nano-OSEDiff (Ours)	24.29	0.628	0.296	27.46	4.92	66.41	1	340	448
Nano-S3Diff (Ours)	23.13	0.573	0.278	22.34	4.09	70.44	1	285	318

Table 11. Quantitative comparison of different methods on real-world datasets. The best, second-best and third-best results are highlighted in red, blue, and green colors, respectively.

Datasets	DRealSR [46]					RealSR [4]				
	Method	PSNR↑	SSIM↑	LPIPS↓	FID↓	MUSIQ↑	PSNR↑	SSIM↑	LPIPS↓	FID↓
SinSR [44]	28.36	0.751	0.366	170.5	55.33	26.28	0.734	0.318	135.9	60.80
OSEDiff [47]	27.92	0.783	0.296	135.3	64.65	25.15	0.734	0.292	123.4	69.09
S3Diff [55]	27.39	0.746	0.312	119.2	64.16	25.19	0.731	0.270	110.3	67.92
Edge-SD-SR [12]	-	-	0.292	-	55.66	-	-	0.278	-	65.20
AdcSR [5]	28.10	0.772	0.304	134.0	66.26	25.47	0.730	0.288	118.4	69.90
TinySR [8]	27.48	0.745	0.311	146.7	65.36	24.79	0.717	0.280	118	69.78
PocketSR [39]	28.05	0.767	0.296	-	63.85	25.47	0.733	0.271	-	67.07
Nano-OSEDiff	29.01	0.808	0.276	134.6	58.84	26.19	0.746	0.272	122.7	65.29
Nano-S3Diff	26.96	0.735	0.321	127.1	67.83	24.47	0.701	0.281	116.8	70.27

## 11.2. Edge Efficient OSEDiff and S3Diff for Single Image Super-resolution

This paper aims to enable real-time super-resolution by effectively harnessing the rich generative priors inherent in pre-trained diffusion models. We validate the efficacy of the proposed foundation model for edge-efficient SR tasks by integrating NanoSD with prominent one-step latent diffusion frameworks, namely OSEDiff and S3Diff.

OSEDiff employs LoRA layers integrated into the VAE encoder and diffusion UNet to perform super-resolution, thereby preserving the prior knowledge of the T2I model. We substitute the latent diffusion model in OSEDiff with NanoSD and fine-tune the asymmetric VAE encoder and UNet using LoRA, setting the rank to 4. Training follows the VSD framework consistent with OSEDiff. In contrast, S3Diff incorporates a pre-trained degradation estimation network to leverage rich content information from LR images. Its diffusion UNet is trained with a degradation-guided LoRA module and adversarial distillation for one-

step SR. We integrate NanoSD into S3Diff, configuring rank parameters for the VAE encoder and diffusion UNet as 16 and 32, respectively, and adhere to S3Diff’s training protocols.

Table 10 and Table 11 present quantitative comparisons of super-resolution methods across three datasets. Both proposed models demonstrate robust performance and computational efficiency. Specifically, they exhibit the second-lowest MACs among evaluated approaches, enabling real-time processing and edge deployment. Nano-S3Diff achieves top NIQE and MUSIQ scores, along with second-best FID results, reflecting superior perceptual quality. Meanwhile, Nano-OSEDiff maintains competitive fidelity, yielding the superior PSNR and SSIM performance over Edge-SD-SR, PocketSR, and AdcSR while surpassing more computationally intensive methods.

Fig. 11 and Fig. 12 present qualitative comparisons between different super-resolution methods. Our proposed approaches demonstrate consistent performance in preserving



Figure 10. Ablation demonstrating the effect of reintroducing the E4--Mid--D4 blocks into NanoSD 1. Column 1: NanoSD 1 and Column 2: NanoSD 1 + E4--Mid--D4. Although these additional blocks significantly increase the parameter count (309 M  $\rightarrow$  565 M), the latency impact is minimal (41 ms  $\rightarrow$  46 ms), since they operate at low spatial resolution. However, as illustrated, the pre-finetuning image quality is nearly unchanged, showing that the large memory overhead provides no practical benefit. This justifies eliminating E4--Mid--D4 from our search space for improved edge efficiency.

image fidelity and reconstructing fine details. In the first example, both Nano-OSEDiff and Nano-S3Diff accurately

reconstruct the striped pattern, while AdCSR generates artifacts and unrealistic textures. The second example shows that our methods effectively restore person details, outperforming AdCSR in terms of both face restoration, structure recovery and detail preservation. These visual results confirm that our edge-efficient models achieve high-quality reconstructions while maintaining rich textural details across various image contexts.

### 11.3. Edge Efficient OSDFace for Face Restoration

This section evaluates the applicability of our proposed model for face restoration tasks. To demonstrate its effectiveness, we integrate NanoSD into the OSDFace framework, which represents the current state-of-the-art one-step diffusion approach for face restoration.

OSDFace acquires comprehensive facial prior features to guide the diffusion process. These priors are generated by training a Visual Representation Embedder (VRE) on low-quality (LQ) facial images. This prior knowledge is integrated into the diffusion UNet using cross-attention layers, with model fine-tuning accomplished via LoRA. To optimize inference speed, NanoSD is incorporated into the OSDFace framework. This implementation retains VRE for prompt embedding construction and employs LoRA-based UNet fine-tuning at a rank of 32. Table 12 and Fig. 13 present comparisons of various methods on three real-world datasets, where our method consistently delivers competitive results. These findings demonstrate that Nano-OSDFace achieves substantial improvements in efficiency while maintaining performance parity with leading face restoration approaches.

### 11.4. Accelerating Diff-Plugin for Image Restoration with Generative Diffusion Prior

The Diff-Plugin framework employs task-specific priors that combine task guidance and input image spatial information. These priors enable pre-trained diffusion models to address low-level vision tasks while preserving content fidelity. Central to this approach is a lightweight Task-Plugin module, which comprises two components: the Task-Prompt Branch (TPB) for task-specific direction and the Spatial Complement Branch (SCB) for enhancing output fidelity through visual guidance. In our implementation, we substitute the original latent diffusion backbone with NanoSD. Task-specific priors extracted by the Task-Plugin are injected into NanoSD’s ResNet and Cross-Attention blocks. Similar to the standard Diff-Plugin framework, the module is optimized using a denoising loss to effectively integrate task-specific guidance into the diffusion process. Fig. 14 and Fig. 15 illustrate the enhanced performance of Nano-Diff-Plugin across four challenging low-level vision tasks. Visual comparisons reveal that our lightweight approach delivers consistent results across all evaluated tasks.

Table 12. Quantitative comparison of different methods on various real-world datasets. The best, second-best and third-best results are highlighted in red, blue, and green colors, respectively.

Method	Wider-Test [61]			LFW-Test [14]			WebPhoto-Test [43]		
	MUSIQ↑	NIQE↓	FID↓	MUSIQ↑	NIQE↓	FID↓	MUSIQ↑	NIQE↓	FID↓
PGDiff [49]	68.13	<b>3.93</b>	35.86	71.24	4.01	<b>41.20</b>	68.59	<b>3.99</b>	<b>86.95</b>
DifFace [52]	64.90	4.23	37.09	69.61	<b>3.90</b>	46.12	65.11	4.24	79.55
DiffBIR [25]	<b>75.32</b>	5.59	35.34	<b>76.42</b>	5.67	<b>40.32</b>	72.27	6.00	<b>91.83</b>
OSEDiff [47]	70.55	4.93	50.27	73.40	4.71	57.80	72.59	5.26	117.5
OSDFace [41]	<b>74.60</b>	<b>3.77</b>	<b>34.64</b>	<b>75.35</b>	<b>3.87</b>	51.04	<b>73.93</b>	<b>3.98</b>	84.59
Nano-DiffBIR (Ours)	<b>74.88</b>	5.73	<b>35.13</b>	<b>76.02</b>	5.81	<b>40.45</b>	<b>72.99</b>	5.89	<b>90.48</b>
Nano-OSDFace (Ours)	74.32	<b>3.96</b>	<b>35.19</b>	75.28	<b>3.81</b>	53.21	<b>74.96</b>	<b>4.01</b>	85.03



Figure 11. Qualitative comparisons of different SR methods. Please zoom in for a better view



LQ

OSEDiff

S3Diff



ADCSR

Nano-OSEDiff

Nano-S3Diff



LQ

OSEDiff

S3Diff



ADCSR

Nano-OSEDiff

Nano-S3Diff

Figure 12. Qualitative comparisons of different SR methods. Please zoom in for a better view

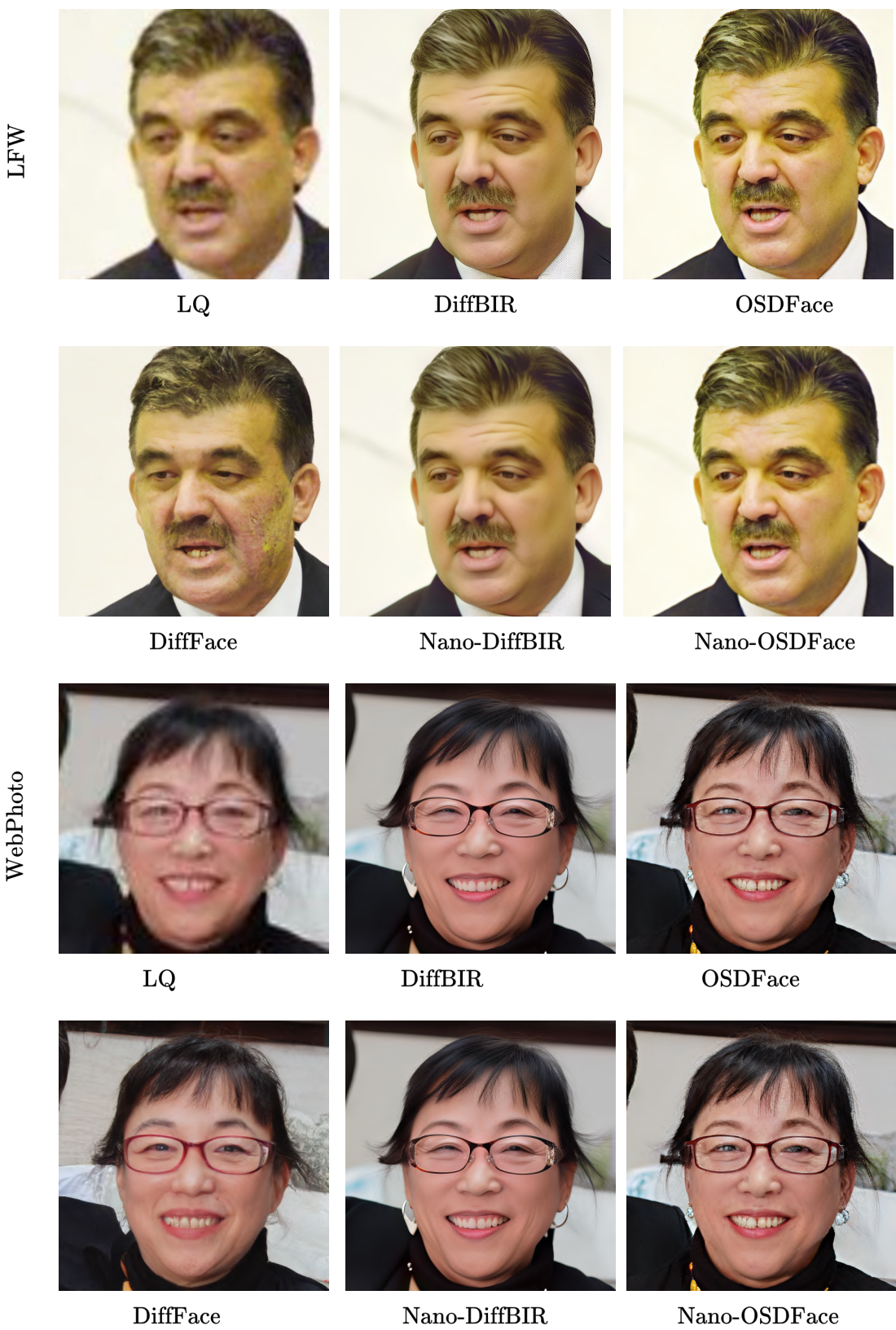


Figure 13. Qualitative comparisons of different FR methods.

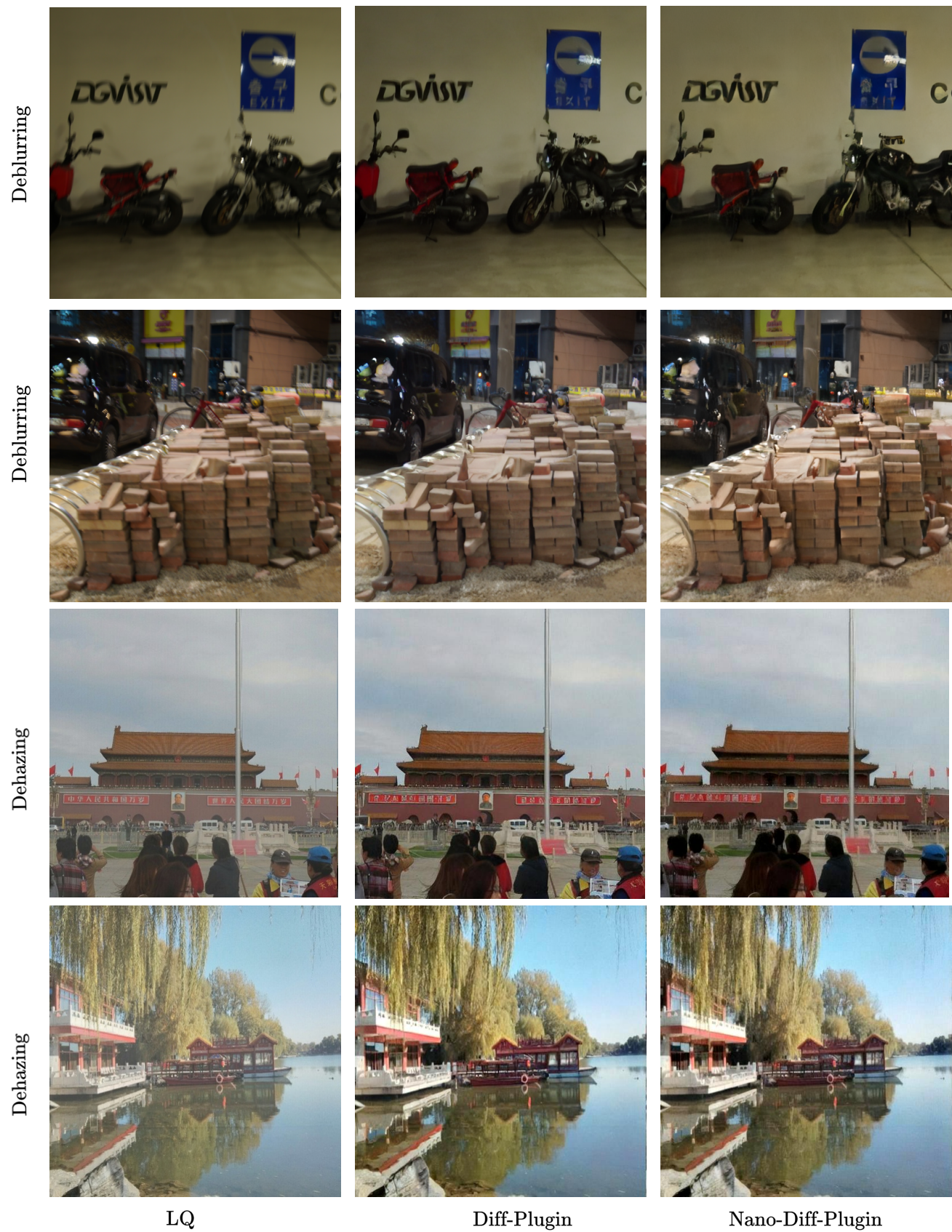


Figure 14. Qualitative comparisons of different methods for various restoration tasks



Figure 15. Qualitative comparisons of different methods for various restoration tasks